NORTHWESTERN UNIVERSITY

Improved Antihydrogen Production at the ATRAP Experiment

A DISSERTATION

SUBMITTED TO THE GRADUATE SCHOOL
IN PARTIAL FULFILLMENT OF THE REQUIREMENTS

for the degree

DOCTOR OF PHILOSOPHY

Field of Physics

By

Edouard Nottet

EVANSTON, ILLINOIS

June 2020

Thesis advisor

Gerald Gabrielse

Author

Edouard Nottet

Improved Antihydrogen Production at the ATRAP Experiment

Abstract

In 2018, our ATRAP collaboration produced 5 trapped antihydrogen atoms per hour long trial. An apparatus with a Ioffe octupole trap and a faster magnet dump was used to confine and detect trapped $\bar{H}$ atoms. This apparatus is unique in that four sideports spaced at 90 degrees from each other around the Ioffe trap provide optical access to the center of the trap to allow precise measurements of the 1S-2S transition of $\bar{H}$ atoms. In a Penning-Ioffe trap, positron and antiproton plasmas on axis at very low temperature with a certain radius, length and density can form trapped antihydrogen atoms via three-body recombination. The strong-drive evaporative cooling method implemented in 2018 is essential to form reproducible plasmas. To better characterize positron, electron and antiproton plasmas, the plasma imaging system was developed and the plasma modes system has been improved. With minor modifications of the apparatus, we would be able to produce and accumulate antihydrogen atoms much faster in the future. For this reason, a new design of the electrode stack is proposed. The accumulation of antihydrogen atoms is essential to trap more than 100 $\bar{H}$ atoms in a Ioffe trap and measure precisely the 1S-2S transition.

Acknowledgments

First, I would like to thank my supervisor Gerald Gabrielse for giving me the opportunity to be part of the ATRAP experiment and for his support during my PhD. He was always present if I needed help at Northwestern or at CERN. His dedication to the ATRAP experiment was very impressive. I also would like to thank my fellow graduate student Nathan Jones. He taught me how to run the experiment at CERN, plasma physics, and to solve electronic problems. We exchanged many emails and calls during the day and the night. Finally, I would like to thank Eric Tardiff, Gunn Khatri, Tharon Morrison, and Daniel Zambrano. Their help was very useful when learning about positrons, lasers, cryogenic systems, and detectors.

Contents

Publications

1. **Lyman-α source for laser cooling antihydrogen**
   G. Gabrielse, B. Glowacz, D. Grzonka, C. D. Hamley, E. A. Hessels, N. Jones, G. Khatri, S. A. Lee, C. Meisenhelder, T. Morrison, E. Nottet, C. Rasor, S. Ronald, T. Skinner, C. H. Storry, E. Tardiff, D. Yost, D. Martinez Zambrano, and M. Zielinski, *Opt. Lett.* **43**, 2905-2908 (2018).

2. **Two-Symmetry Penning-Ioffe Trap for Antihydrogen Cooling and Spectroscopy**
   E. Tardiff, X. Fan, G. Gabrielse, D. Grzonka, C. Hamley, E. A. Hessels, N. Jones, G. Khatri, S. Kolthammer, D. Martinez Zambrano, C. Meisenhelder, T. Morrison, E. Nottet, E. Novitski and C. H. Storry, arXiv:2003.05032 (2020).

Chapter 1

Introduction

1.1 CPT theorem and antihydrogen experiment

1.1.1 The CPT theorem

It is still unknown why matter, rather than antimatter, survived after the big-bang. One of the explanations could be that the matter-antimatter asymmetry in the universe could be generated through CPT violation and baryon number violation. The CPT theorem suggests that every relativistic quantum field theory has a symmetry that simultaneously reverses charge, reverses the orientation of space and reverses the flow of time [1]. CPT symmetry is one of the most important fundamental property of relativistic quantum field theory. No experiments have so far found a CPT violation. However, some string theories violate CPT symmetry [2] and gravity has not yet been successfully described by a quantum field theory. It is possible that the CPT theorem is not universal.

P, C and T symmetries are all separately violated. For examples, Wu et al. observed in 1956 the first experimental evidence of parity violation during the β decay of spin-polarized ${}^{60}_{27}\mathrm{Co} \rightarrow {}^{60}_{28}\mathrm{Ni} + e^- + \bar{\nu}_e + 2\gamma$ [3]. Equal numbers of electrons should be emitted parallel and antiparallel to the magnetic field if parity is conserved. But they found that more electrons were emitted in the direction opposite to the magnetic field and therefore opposite to the nuclear spin. Then, CP violation was discovered in 1964 by Cronin and Fitch [4]. Neutral kaons can ever decay into pions, positrons and neutrinos or into pions, electrons and anti-neutrinos. However, they observed that such transformations do not occur with the same probability in both directions. CP invariance suggests an identical probability for the two, contrary to observations.

1.1.2 Comparison of the 1S-2S transition of hydrogen and antihydrogen atoms

Studies on trapped antihydrogen atoms will give the possibility to answer the following question in physics: is CPT symmetry an exact symmetry of nature? By comparing the 1S-2S transition of antihydrogen and hydrogen atoms, it is possible to test CPT invariance in this system. CPT invariance implies that particles and antiparticles have the same mass, magnetic moment (except opposite sign), mean life and charge-to-mass (except opposite sign). It also implies that H and $\bar{H}$ have the same atomic structure and transition frequencies. Different experiments compare energy levels, magnetic moments, mass ratios, charge-to-mass ratio and lifetime of different types of particles (lepton, baryon and meson) to test CPT invariance at various precision (Fig 1.1). The precision that could be achieved by comparing the

$\bar{H}$ and H 1S-2S transition frequency is very high if the $\bar{H}$ transition can be measured as precisely as with H (Fig 1.1). The 1S-2S transition of hydrogen atoms has been already measured very precisely: $f_{1S-2S} = 2.46 \times 10^{15}$ Hz $\pm$ 10 Hz [5]. This represents a fractional uncertainty of 4.2×10^{-15}.

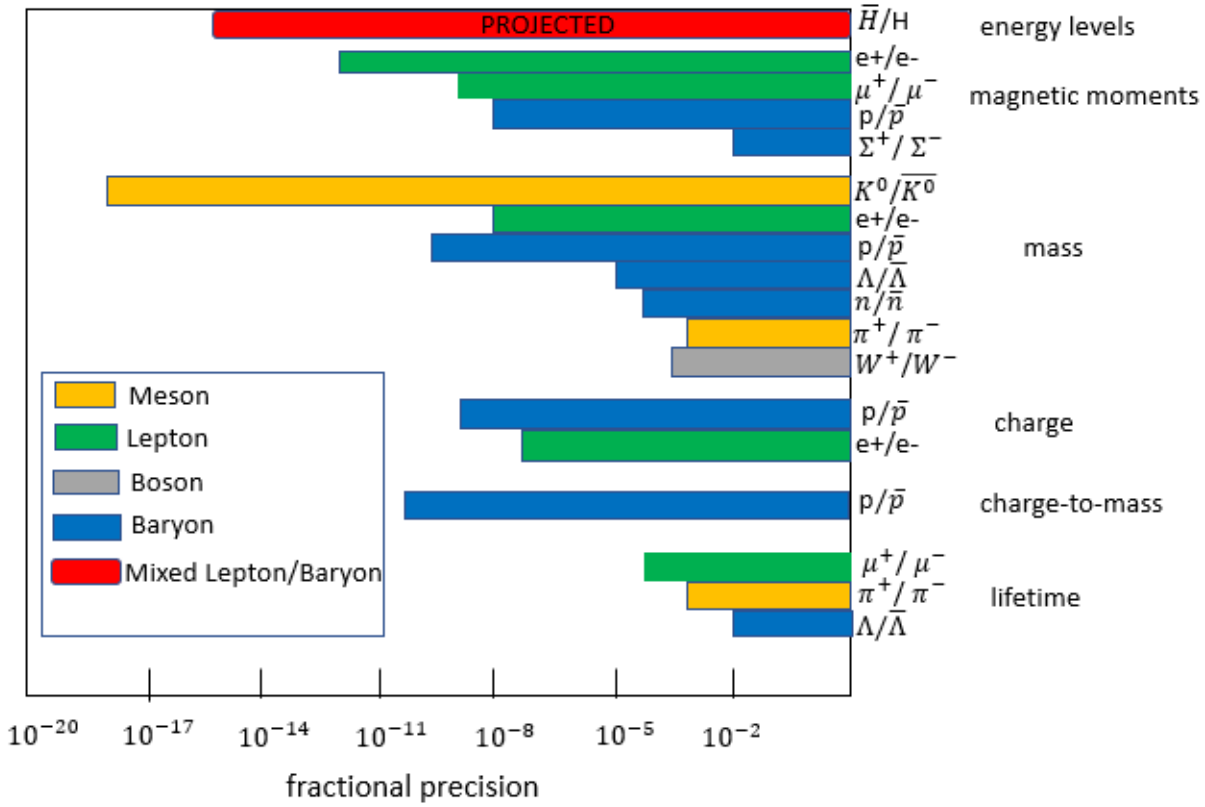

Figure 1.1: CPT tests and comparison of how accurately the 1S-2S transition of $\bar{H}$ and H atoms could be compared if the H precision is attained [6].

A measurement at the hydrogen precision of the lepton-baryon system (Fig 1.1) would improve the lepton and baryon measurements tests. The ratios of m_{e+}/m_{e-} could be improved by a factor of 10000 [7] and $m_{\bar{p}}/m_p$ [8] by an order of magnitude. In fact, the ratio of Rydberg constants determined from the 1S- 2S transition in H and $\bar{H}$ depends on the ratios of the masses and charges of their ingredient particles

$$\frac{R_{\bar{H}}}{R_H} = (\frac{m_{e+}}{m_{e-}})(\frac{q_{e+}}{q_{e-}})^2(\frac{q_{\bar{p}}}{q_p})^2(\frac{1+m_{e-}/m_p}{1+m_{e+}/m_{\bar{p}}}). \tag{1.1}$$

However, no precise measurement of the $\bar{H}$ 1S-2S transition has been determined. The only $\bar{H}$ 1S-2S transition measurement, made in 2018 by the ALPHA experiment, had the following result, $f_{1S_d-2S_d} = 2.46 \times 10^{15}$ Hz $\pm$ 5 kHz [9]. The big uncertainty of this measurement is due to the trap environment and due to the number of antihydrogen atoms. The corresponding hydrogen transition was not measured in the same environment, as must happen to reliably determine the uncertainty. Velocity-dependent systematic shifts, such as transit-time broadening, could be reduced when using the lyman-alpha laser, which should slow down and cool antihydrogen atoms to very low temperatures. This process will be explained in more details in chapter 2. But the Zeeman shift and the D.C. Stark shift are specific to the trap environment where $\bar{H}$ atoms are formed and induce uncertainties to the final measurement. One way to reduce these shifts would be to compare the 1S-2S transition of H and $\bar{H}$ atoms in the same environment. Finally, the ALPHA experiment used a total of 15 000 trapped antihydrogen atoms [9] for this measurement. This is small in comparison to 10^{12} atoms usually used to measure the 1S-2S transition of hydrogen atoms.

1.1.3 Spectroscopy

The ATRAP experiment seeks to test CPT invariance by comparing the 1S-2S transition of $\bar{H}$ and H atoms. To excite the 1S-2S transition of antihydrogen atoms, we send a continuous-wave light from a 243-nm laser (explained in chapter 2) into a cavity surrounding the trapping volume. Two counter-propagating photons can

resonantly excite the ground-state atoms to the 2S state (Fig 1.2).

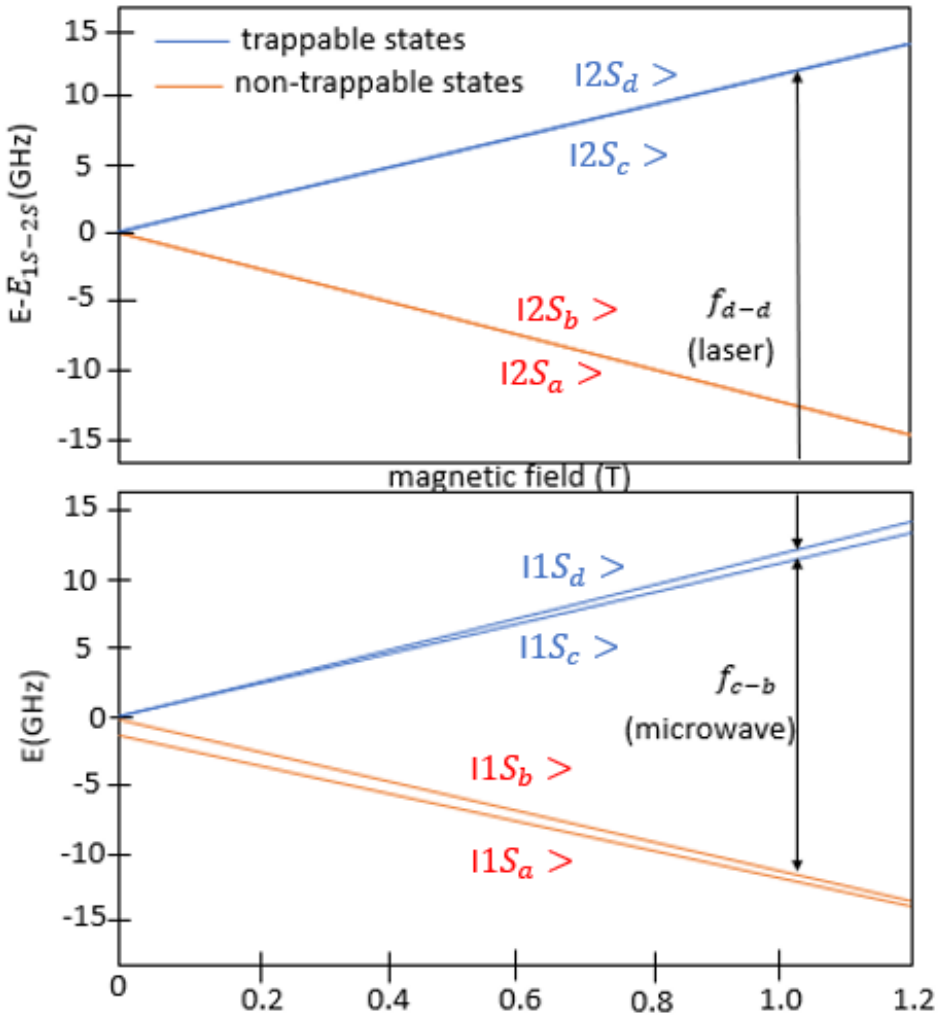

Figure 1.2: 1S-2S transition frequency.

Antihydrogen atoms can be trapped in the $1S_c$ and $1S_d$ states (explained in chapter 2). The $1S_a$ and $1S_b$ levels are untrappable states (Fig 1.2). Near 1 T, the frequency of the $1S_d$-$2S_d$ transition changes at 961 kHz/T and the frequency of the $1S_c$-$2S_c$ transition changes at 18.6 MHz/T due to Zeeman broadening. By driving out $1S_c$ states with microwaves, we can measure the $1S_d$-$2S_d$ transition (Fig 1.2). Microwaves

can resonantly drive transitions from trapped to un-trapped states. Once antihydrogen atoms are excited to the 2S state, they can evolve in different ways. They can either emit two photons and return to their ground state or absorb another photon, which ionizes the atom or they can emit a single photon and return to the ground state via the 2P state. To measure the 1S-2S transition of antihydrogen atoms, when there is ionization, we detect the maximum antiproton annihilation rate.

1.2 Overview of the antihydrogen research and of this work

After the observation of the first antiproton in 1955 [10], the TRAP collaboration successfully slowed, captured, and cooled antiprotons for the first time in 1986 [11]. Then, in 1989, Gabrielse proposed new methods now used to create [12] and trap antihydrogen atoms for precision spectroscopy and gravitational studies. For these measurements, antiprotons and positrons were captured in a Penning trap to interact and form antihydrogen atoms. The observation of the first cold antihydrogen atoms was shown in 2002 by ATRAP [13] (successor of TRAP) and ATHENA [14] collaborations. Then, in 2004, the expanded ATRAP collaboration found an alternative method to produce cold antihydrogen atoms through laser-controlled charge-exchange collisions [15].

In 2008, the ATRAP collaboration achieved the next milestone by showing the possibility to trap cold antihydrogen atoms using a quadrupole Ioffe trap [16]. The production of $\bar{H}$ atoms in a combined Penning-Ioffe trap was successfully demon-

strated [17]. In 2011, the ALPHA collaboration (successor of ATHENA), reported that they were able to produce and trap 1 $\bar{H}$ atom per trial [18] for up to 1000 s in a Ioffe trap. In 2012, the ATRAP collaboration produced 5 trapped $\bar{H}$ atoms per trial (every 2 hours) for up to 1000 s [19].

To increase the number of trapped antihydrogen atoms produced per trial, several plasmas diagnostics [20] and plasma manipulation techniques [21] were successfully implemented at the ATRAP experiment. The ALPHA experiment developed other methods, such as the accumulation method, to trap many antihydrogen atoms. In 5 consecutive trials, they were able to accumulate 54 trapped antihydrogen atoms [22]. As a consequence, in 2018, the ALPHA experiment reported their first measurement of the 1S-2S transition of $\bar{H}$ atoms [9].

From 2012 to 2015, the ATRAP experiment designed a new apparatus [23]. This new apparatus has a deeper Ioffe quadrupole trap, a Ioffe octupole trap and a faster magnet dump [24]. The design of the Ioffe trap allows to laser-cool antihydrogen atoms. From 2016 to 2018, before the CERN long shutdown, the main goal of the ATRAP experiment was to improve plasma diagnostics and plasma manipulation techniques to form trapped antihydrogen atoms with the new apparatus and demonstrate laser-cooling.

After this introduction, in **chapter 2**, the new cryogenic apparatus and methods to measure the 1S-2S transition of antihydrogen atoms will be presented. In addition, we will describe the Lyman-alpha laser system at the ATRAP experiment.

In **chapter 3**, we will see how non-neutral plasmas are formed at CERN. In the apparatus, most of antihydrogen atoms are produced via three-body recombination.

The temperature, the density and the geometry of plasmas are essential parameters for the antihydrogen production. For this reason, plasmas diagnostics were improved to characterize effectively non-neutral plasmas. The plasma imaging system was implemented for the first time at the ATRAP experiment in 2018. We were able to image and characterize antiproton, positron and electron plasmas. The plasma modes system was also improved at a higher level of precision to characterize electron and positron plasmas with a small number of particles.

In order to form trapped antihydrogen atoms with reproducible plasmas, **chapter 4** describes plasma manipulation techniques such as the strong-drive regime-evaporative cooling method [25]. These techniques were improved with plasma diagnostics. As a result, in 2018, we produced 5 trapped antihydrogen atoms per trial, using an hour long procedure [24].

In **chapter 5**, we show how to re-design the apparatus to accumulate more than 100 trapped antihydrogen atoms. A new design of the electrode stack is proposed to produce and accumulate antihydrogen atoms much faster.

Chapter 2

The ATRAP apparatus

2.1 The Penning trap

To form trapped antihydrogen atoms at the ATRAP experiment, we use a cryogenic Penning-Ioffe trap (Fig 2.1) to confine charged electrons, positrons or antiprotons, and neutral antihydrogen atoms. The Penning trap confines charged particles. In the ideal case, a uniform axial magnetic field $\vec{B} = B_0\hat{z}$ provides a radial confinement and biased electrodes provide an electrostatic axial confinement (Fig 2.1) with a quadrupole potential

$$\phi(\rho, z) = \frac{V_0}{2d^2}(z^2 - \frac{\rho^2}{2}). \tag{2.1}$$

Here $d = \frac{1}{2}(z_0^2 + \frac{\rho_0^2}{2})$ is a geometrical factor, z_0 is the electrode half-height, and ρ_0 is the electrode radius.

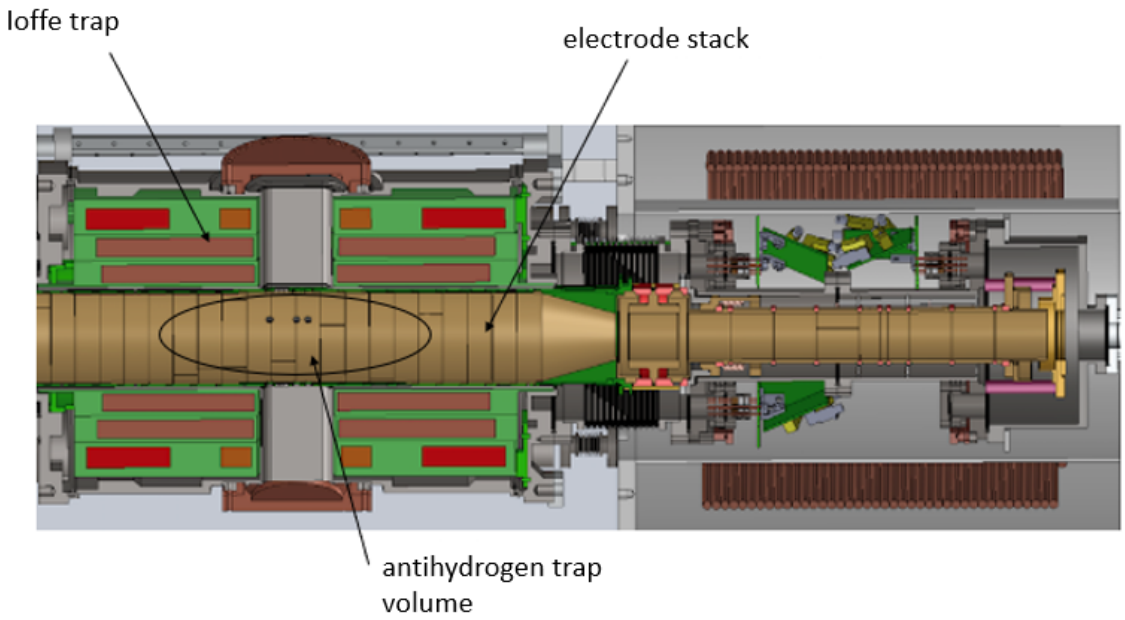

Figure 2.1: Nested Penning-Ioffe trap.

The motion of particles in a Penning trap is governed by the Lorentz force, $\vec{F} = q(\vec{E} + \vec{v} \times \vec{B})$. The equations of motion for a particle of charge q and mass m in an ideal Penning trap are

$$m\ddot{x} = \frac{qV_0}{2d^2}x + qv_yB_0 \tag{2.2}$$

$$m\ddot{y} = \frac{qV_0}{2d^2}y - qv_xB_0 \tag{2.3}$$

$$m\ddot{z} = \frac{-qV_0}{d^2}. \tag{2.4}$$

The first two of these equations can also be written using $u \equiv x + iy$ as

$$\ddot{u} + i\omega_c\dot{u} - \frac{1}{2}\omega_z^2 u = 0, \tag{2.5}$$

where $\omega_c = \frac{qB_0}{m}$ and $\omega_z = \sqrt{qV_0/md^2}$.

This differential equation has a general solution of the form $u = e^{-i\omega_\pm t}$

$$\omega_{\pm} = \frac{1}{2}(\omega_c \pm \sqrt{\omega_c^2 - 2\omega_z^2}). \tag{2.6}$$

Based on the previous expression, particles inside the Penning trap execute several motion: the axial motion at frequency ω_z, the cyclotron motion at frequency ω_+ and the magnetron motion at frequency ω_- (Fig 2.2).

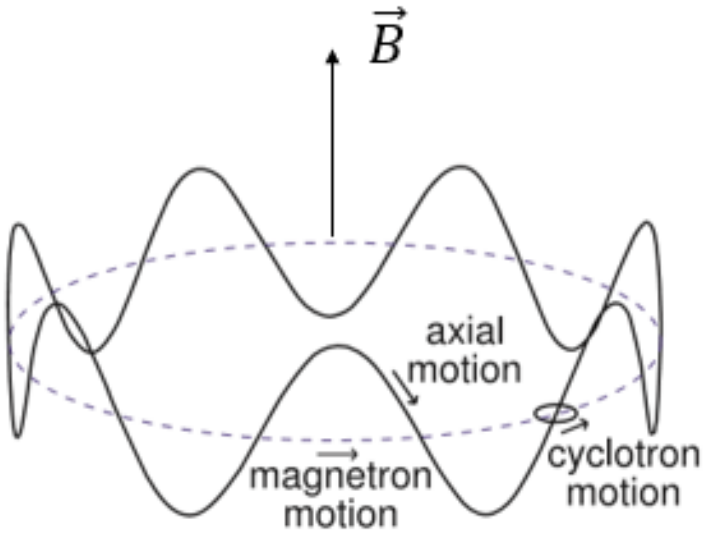

Figure 2.2: Particle motions in a Penning trap [26].

The cyclotron motion at a frequency near the free space cyclotron frequency ω_c confines the particles radially, but they are free to move along the direction of the magnetic field. The axial motion at a frequency ω_z corresponds to a harmonic oscillation of the particles. The axial frequency is also called the center-of-mass (COM) mode of a plasma. For a charged particle to remain stable, the oscillation frequencies $\omega_{\pm}$ must be real, which requires $\omega_c \geq \sqrt{2}\omega_z$. In this limit, the modified cyclotron frequency $\omega_+ = \omega_c - \omega_m$ and $\omega_- \approx (\omega_z^2/2\omega_c) = \omega_m$ is the magnetron frequency. The magnetron motion corresponds to a drift of the cyclotron center along the electric

equipotential lines perpendicular to the magnetic field direction.

2.2 The electrodes

To manipulate charged particles, we use Penning trap geometries with compensated cylindrical electrodes and open endcaps [27]. With this geometry, positrons and antiprotons can access the long trap from the top and the bottom at the same time (Fig 2.4). With these electrodes, we form nested wells to mix antiprotons and positrons in the upper trap to produce trapped antihydrogen atoms (Fig 2.4). However, to form harmonic potentials within a cylindrical electrode stack, it is useful to know by how much a cylindrical potential differs from an ideal quadrupole. For this reason, we expand the general potential in terms of legendre polynomials in spherical coordinates

$$\phi(r,\theta) = \frac{Vo}{2}\sum_{j=0}^{\infty} Cj(\frac{r}{d})^j Pj(cos\theta). \tag{2.7}$$

C_j represents the size of harmonic (j=2) and anharmonic (j>2) terms in the expansion (Fig 2.3).

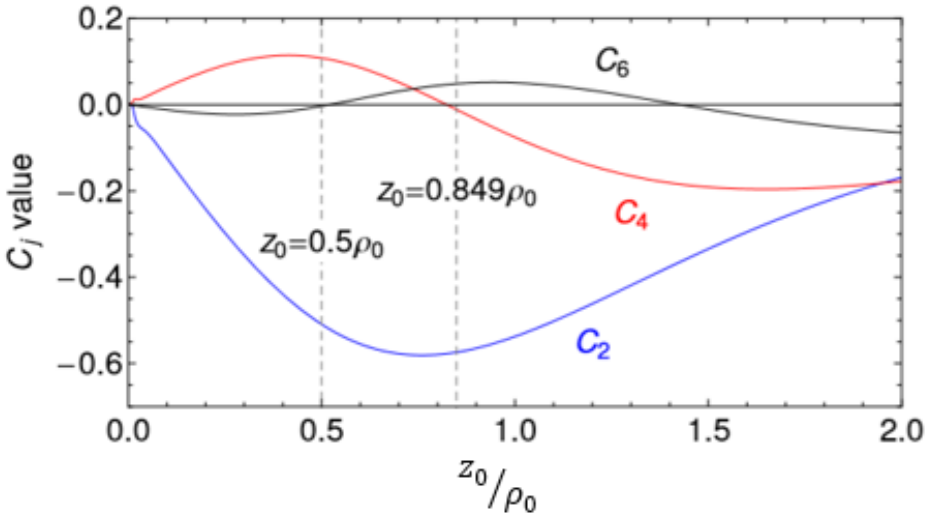

Figure 2.3: Coefficients for a cylindrical electrode in a 3 electrodes trap as a function of electrode length [20]. Perfect electrodes are assumed.

In the lower electrode stack (Fig 2.4), each electrode minimizes the first anharmonic correction, $z_0 = 0.854\rho_0$ (Fig 2.3). Electrodes in the upper stack (Fig 2.4) have a half-length $z_0 = 0.257\rho_0$ which do not minimize the first anharmonic term. However, by appropriately biasing multiple upper stack electrodes at the same time, we can form better harmonic potentials.

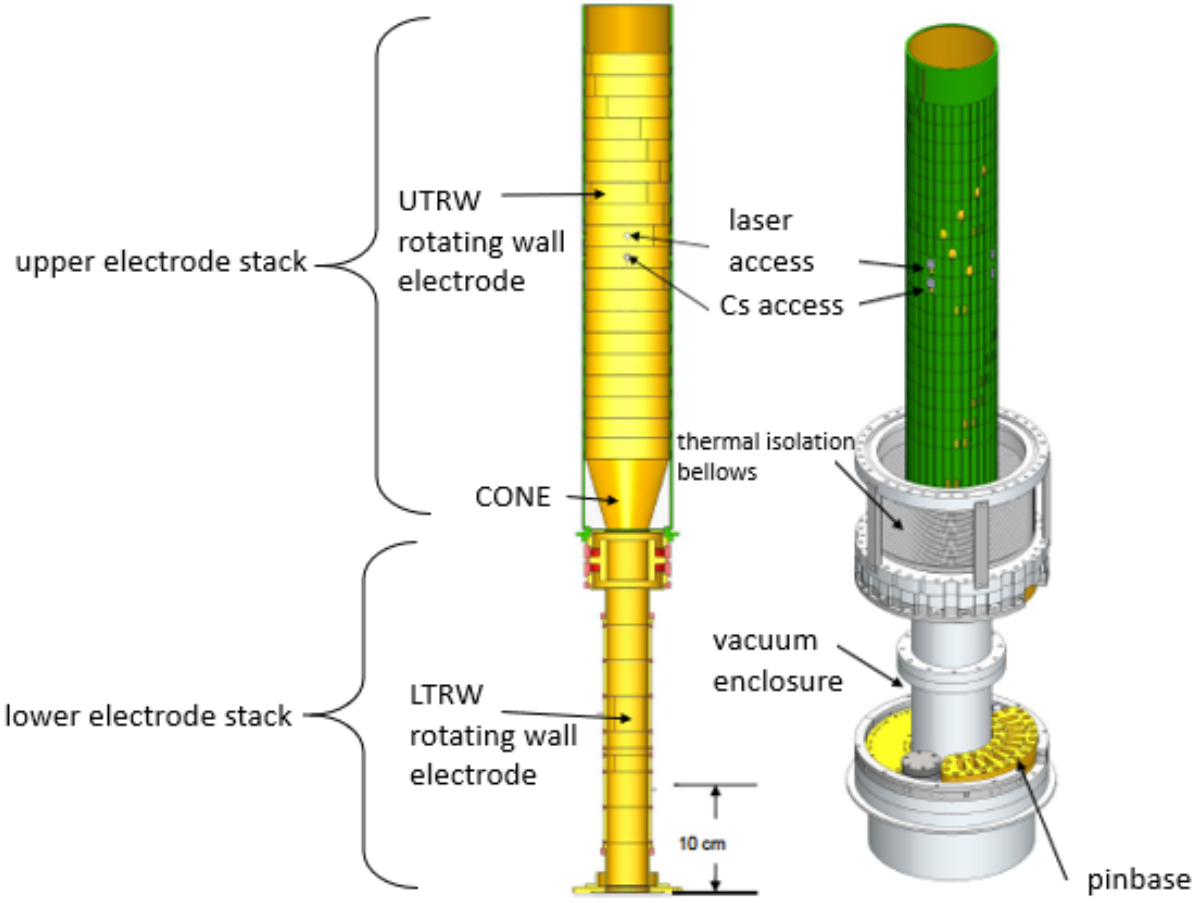

Figure 2.4: CTRAP electrode stack.

Electrodes in the upper stack (68 mm diameter, 17.3 mm length) are twice bigger in diameter than electrodes in the lower stack (35 mm diameter, 30.7 mm length) to increase the trap depth of the Ioffe trap (explained later in this chapter). Between the lower part and the upper part of the electrode stack, there is a CONE electrode (Fig 2.4). Plasmas are transfered smoothly from the lower trap to the upper trap with the CONE electrode. To measure the 1S-2S transition of antihydrogen atoms, some of the electrodes have holes for laser access near the Ioffe trap region (Fig 2.4). Finally, two rotating wall electrodes LTRW and UTRW are used to compress or expand plasmas

using a rotating electric field (Fig 2.4), in the lower trap and in the upper trap. More details about rotating wall electrodes will be discussed in chapter 4.

All electrodes can be biased with DC voltages, and most can also receive pulsed RF voltages. Signals travel through feedthroughs, then through the insert dewar vacuum space (Fig 2.8) up to the electrode stack pinbase flanges (Fig 2.5). The pinbases contain electrical feedthroughs which enter the experiment vacuum space. In order to limit noise inside of the electrode stack, signals are filtered at the pinbase before going to the electrodes. There are three filter boards, two for the upper stack and one for the lower stack (Fig 2.5). Most of the RF signals are pulses from high voltage pulsers with 50 ohms output impedance. The low-voltage DC signals comes from high-precision voltage amplifiers. The maximum voltage used to bias normal electrodes is $\pm$ 600V.

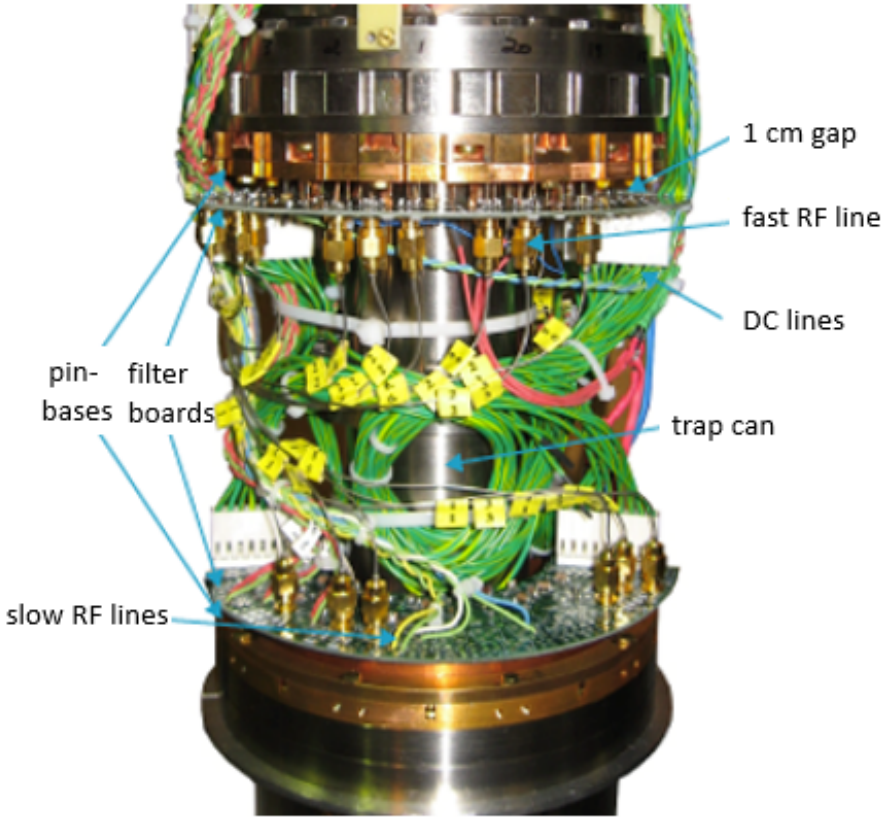

Figure 2.5: CTRAP electrodes wiring.

2.3 Ioffe trap

Once plasmas are prepared in the electrode stack at a given temperature, density, and geometry (as we will see in chapter 3) positron and antiproton plasmas mix together to form antihydrogen atoms. Some of the $\bar{H}$ atoms will remain confined in the Ioffe trap (Fig 2.1). An antihydrogen atom has an intrinsic magnetic dipole moment due to the spin of the positron and the orbital motion of the positron. If the antihydrogen atom is in its ground state, the orbital angular momentum is equal to zero and only the positron spin angular momentum contributes to the atom magnetic

dipole moment. Antihydrogen atoms can be trapped in a magnetic minimum if they occupy low-field seeking states. A magnetic dipole moment which is anti-parallel to the magnetic field is called a low-field seeker. The magnetic moment $\vec{\mu}$ and spin $\vec{S}$ are co-aligned for a positron, so the low-field seeking states in $\bar{H}$ have $m_j = -1/2$. The potential energy of a magnetic moment in a magnetic field is equal to $U = \vec{\mu} \cdot \vec{B}$. Low-field seekers have potential energies that increase with the magnetic field (Fig 1.2). Such particles are attracted to regions with a low magnetic field strength. These levels are called trappable states. On the contrary, high-field seekers have potential energies that decrease with the magnetic field. High-field seeking particles cannot be trapped because it is impossible to create a static magnetic field maximum in free space.

In general, a Ioffe trap may be created from four current-carrying bars [24]. Four straight bars with alternating directions of current flow form a radial quadrupole and two pinch coils form an axial well (Fig 2.6). Higher-order Ioffe traps are also possible, for which the number of straight bars is increased [24]. A bucking coil is also used to flattens out the trap and to form a deeper and more homogenous trap (Fig 2.6). Four sideports spaced at 90 degrees from each other provide optical access to the center of the trap to measure the 1S-2S transition and laser-cool antihydrogen atoms (Fig 2.6).

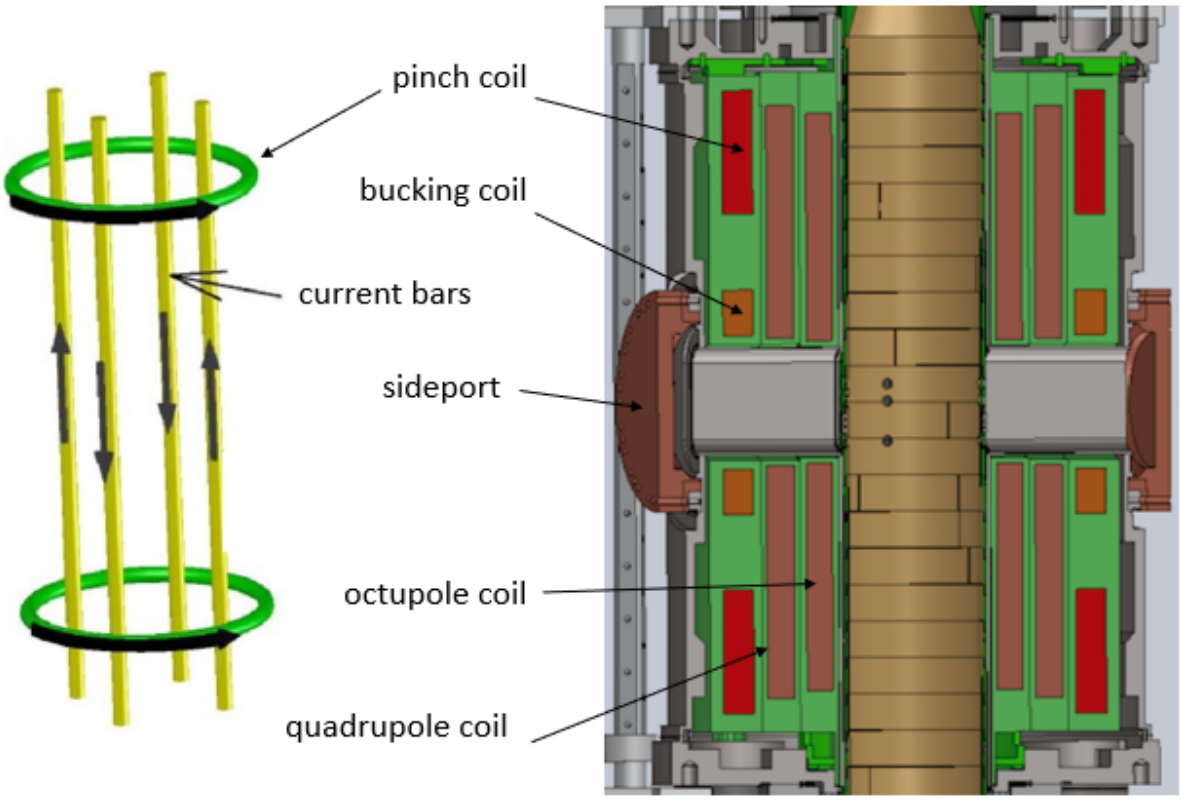

Figure 2.6: Ioffe trap cross section.

The trap depth of the Ioffe trap is defined as $|\mu|\Delta B$ with ΔB the difference between the minimum $|\vec{B}|$ along the boundary of the trap volume and the minimum $|\vec{B}|$ anywhere in the trap. The trap depth for ground-state atoms in temperature units can also be determined from $T = \mu_B \Delta B / k_B$, where μ_B is the Bohr magnetron. The quadrupole Ioffe trap has a slightly higher trap depth (526 mK) than the octupole trap (405 mK). The quadrupole trap destabilize very quickly away from the axis due to the strong quadrupole field gradient (green curve in Fig 2.7) in comparison to the octupole field gradient (blue curve in Fig 2.7). As we move away from the center of the Ioffe trap, the trap depth decreases.

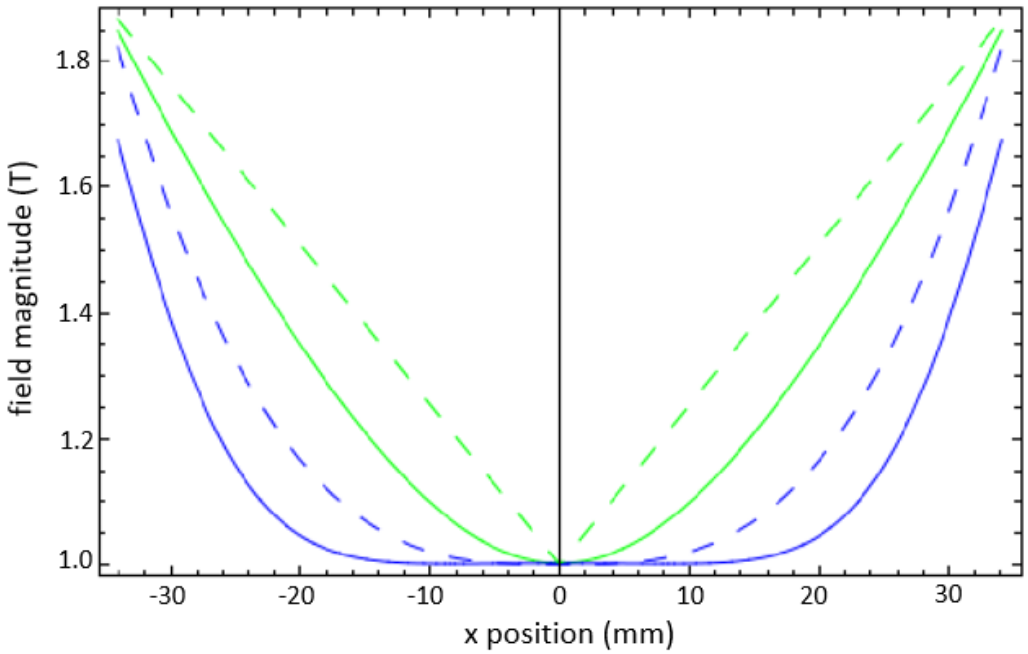

Figure 2.7: Magnetic field gradients due to the Ioffe octupole (blue curve) and quadrupole trap (green curve). Dashed lines represent simulations of these magnetic field gradients for an infinitely long perfect trap.

The Ioffe trap is a low inductance trap. Coils can be turned on in seconds and off in milliseconds. As a consequence, the cosmic ray signals that could be confused with annihilations from $\bar{H}$ are reduced. Fast current measurements indicate that essentially all $\bar{H}$ are released within 50 ms of a triggered current dump, with 94 % of particles leaving radially [24].

2.4 The apparatus

The ATRAP apparatus is made of a Penning-Ioffe trap, cryogenic systems and detectors. The Penning trap has 32 cylindrical electrodes and a 1 T superconducting magnet that surrounds these electrodes (Fig 2.8). Antiprotons enter the bottom

of the electrode stack in a 2.7 T field from a field-boosting solenoid (Fig 2.8) and the 1 T solenoid together. This prevents more $\bar{p}$ from hitting walls than would the 1 T solenoid field alone. Increasing B_0 decreases the antiproton cyclotron radius ($r_c = \sqrt{2mE_c}/qB_0$) and more particles can be trapped.

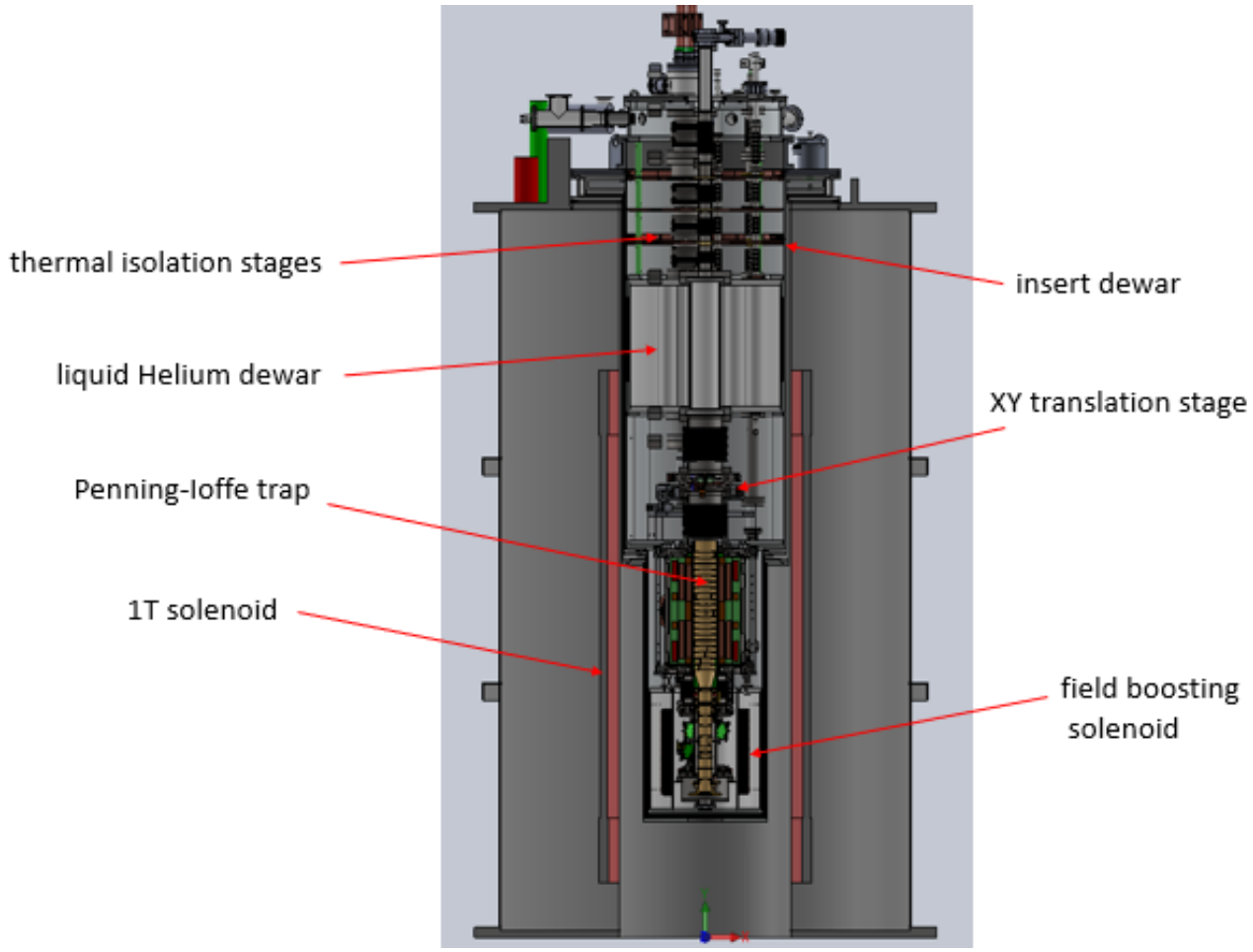

Figure 2.8: Apparatus.

The trap is isolated from room temperature with a vacuum space located between the insert dewar and the apparatus (Fig 2.8). Liquid helium that cools the trap vacuum container to 4.2 K is located in a helium dewar above the trap. To reduce the liquid helium boiloff rate, three thermal isolation stages minimize the radiative

heat load from the top of the experiment. To further reduce the temperature to 1.2 K in the electrode stack, we use a pumped helium-4 system also called 1 K pot. The pressure in the pot is reduced by pumping with an external scroll pump (Edwards XDS-35) [23], reducing the temperature of the liquid helium within to 1.2 K. The 4.2 K helium dewar and the 1 K pot are coupled with a thin-walled titanium impedance line that controls how much helium gets into the 1 K pot. To couple the electrodes to the 1 K pot, copper tubes carry 1.2 K liquid helium along the side of the Ioffe trap and through the gap between the Ioffe trap and the field-boosting solenoid.

Finally, a XY translation stage is placed above the electrode stack (Fig 2.8). The stage allows for various windows and holes to be moved onto the center access of the trap. Using this 2D-XY translation stage, we can image plasmas with the plasma imaging assembly (Fig 2.9) or send the Lyman-alpha laser into the trap via a magnesium fluoride window (Fig 2.9). In 2018, we also added a waveguide on the stage to send microwaves in the experiment space (Fig 2.9). There are 2 holes of 1.5 mm diameter surrounded by faraday cups on the XY translation stage. With the laser hole, at the center, we align and send the excimer laser on axis into the trap. With the positron hole, we align and send positrons into the trap (Fig 2.9). The XY translation stage moves in the X and Y direction under vacuum and at cryogenic temperatures. The motor for the stage are located above the apparatus at room temperature. A pair of 130 µm wall-thickness edge-welded bellows above and below the XY stage keep the trap vacuum intact as the stage moves back and forth.

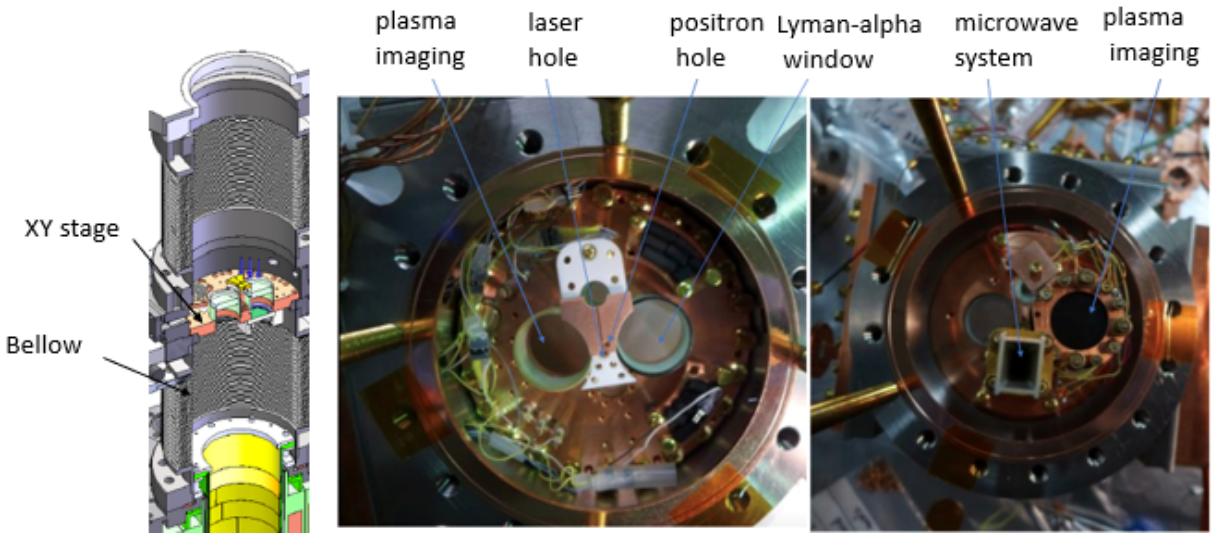

Figure 2.9: XY translation stage.

2.5 Detectors

To detect trapped $\bar{H}$ atoms, positrons or antiprotons, we use scintillating fibers and paddles that surround the apparatus (Fig 2.10). When an antiproton annihilates at a wall, the following reaction is produced $p + \bar{p} \rightarrow 3.0\ \pi^{+-} + 2.0\ \pi^{0}$. Scintillating detectors are sensitive to charged particles. Pions undergo minimum energy loss upon interaction with the scintillators, which measure this energy loss. They are minimum-ionizing particles (MIPs) because their mean kinetic energies of 190 MeV is greater than their rest energy of 140 MeV.

The detector system, at the ATRAP experiment, is composed of 784 flexible scintillating plastic fibers with straight and helical layers surrounding the insert dewar over the Ioffe trap region and 24 plastic double layer scintillating paddles surrounding the 1 T magnet bore [23] (Fig 2.10). There are 8 paddles in an octagonal configuration

on the outer layer and 16 half-sized paddles on the inner layer. All paddles are 1 m height. When charged particles pass through plastic scintillators, they electronically excite atoms/molecules, which release light. Signals received on scintillating fibers and paddles are extracted using PMTs (photomultiplier tubes). These PMTs are connected to discriminators that extract a certain voltage above background (at 470 keV). In general, MIPs (single minimum ionizing particles) such as pions or cosmic muons generate 10k photons in 1 cm of our scintillators.

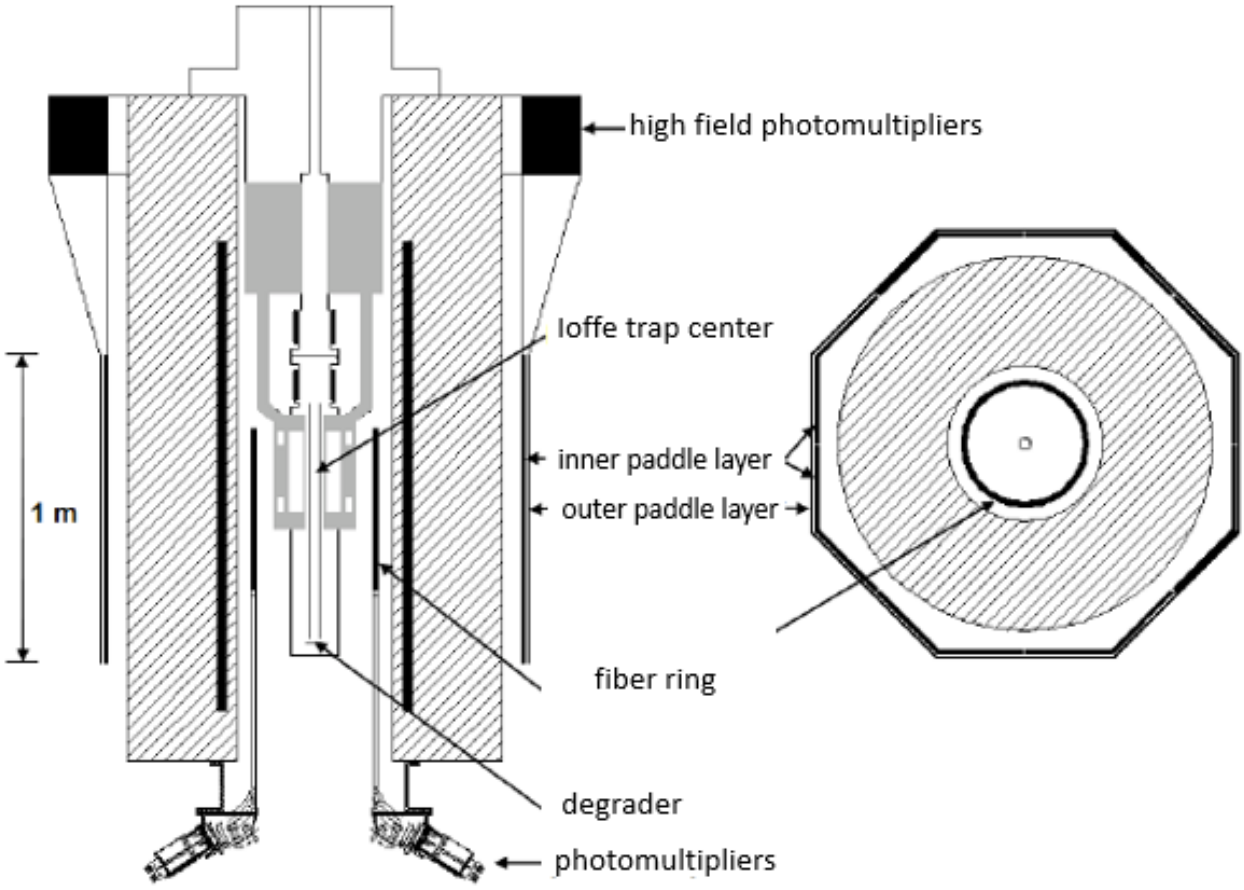

Figure 2.10: Detectors at the ATRAP experiment [20].

To determine MIPs efficiencies for scintillating fibers and paddles, we use high

energy cosmic rays that perpetually bombard our experiment. We observe the likelihood that intermediary fibers and paddles along each straight-line path are triggered which is consistent with a cosmic ray passing through the detector system. The MIPs detection efficiency is 95% for the paddles and 94.5% for the fibers. However, antiprotons can't be directly detected because they annihilate with gold nuclei, create many MIPs [28] and the number varies from annihilation to annihilation. One of the limiting factor of the detector system is the limited solid angle of scintillating fibers and paddles. As a consequence, we use MIP efficiencies, the detector geometry and a Monte Carlo simulation to determine the $\bar{p}$ detection efficiency. The Monte Carlo simulation generates a random number of MIPs based on the properties of antiproton annihilations on a gold surface and sent them in random directions. Based on these informations, the paddles detection efficiency is 68 % and the fibers detection efficiency is 87 % [20]. To improve even more the sensitivity of $\bar{p}$ annihilations, the detector system is calibrated with large numbers of $\bar{p}$ and cosmic rays to find the relative proportion of each event type.

2.6 Laser diagnostics and the microwave system

To measure the 1S-2S transition of antihydrogen atoms with the apparatus, several sytems have been implemented. The ATRAP experiment has a commercial 243 nm laser that provides around 30 mW of average power. First, a 972 nm laser is sent through an ULE cavity to stabilize the laser linewidth. Then, the 972 nm source is frequency doubled in a LBO non-linear crystal to produce the 243 nm wavelength. A cavity formed with mirrors to either side of the Penning-Ioffe trap build up the

power. Two Ioffe trap sideports are used for this purpose (Fig 2.6). To improve the precision of spectroscopic measurements, we want to measure the $1S_d$-$2S_d$ transition of antihydrogen atoms to reduce Zeeman broadening (as explained in chapter 1). For this reason, microwaves are sent into the apparatus via a purpose-built vacuum feedthrough (Fig 2.11), then through a waveguide located on the 2D-XY translation stage (Fig 2.11.B) to the trapping volume (Fig 2.12).

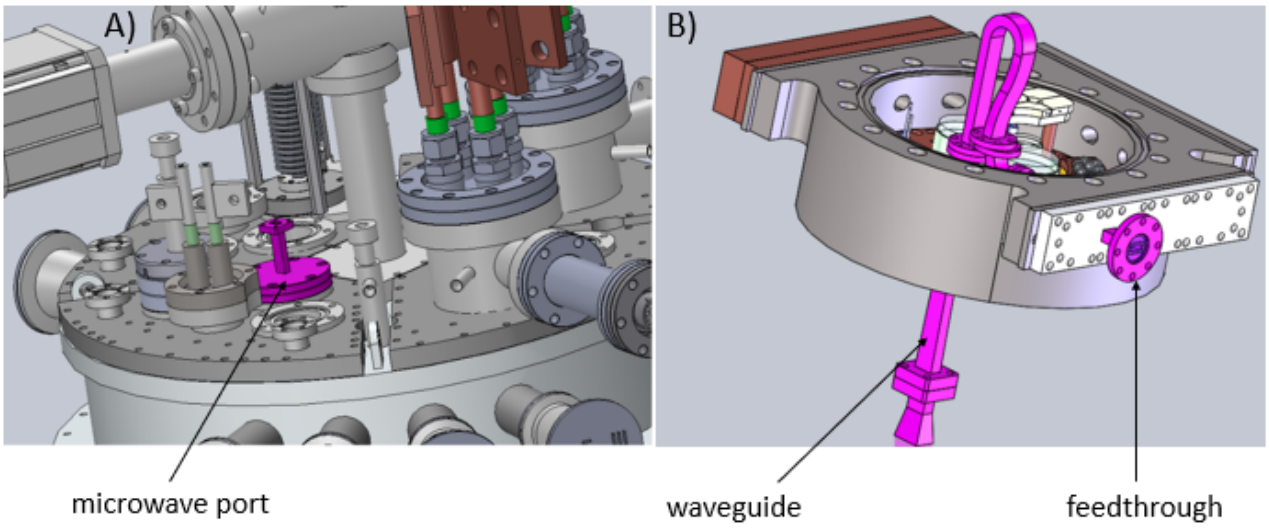

Figure 2.11: The microwave system.

Finally, to reduce broadening effects such as transit-time broadening, we would like to laser-cool trapped antihydrogen atoms. We use the 1S-2P transition at a wavelength of 121.6 nm to laser cool antihydrogen atoms. Doppler cooling of magnetically trapped hydrogen was first reported [29] in 1993 and no other similar experiments have been reported since then. Hour-scale cooling times are reasonable for antihydrogen studies because the high vacuum within the cryogenic apparatus leads to very long trap lifetimes. When laser cooling, atoms traveling toward the laser get a kick in the opposite direction from absorbing a photon and slow down. They do re-emit

a photon, but in a random direction. Consequently, there is a cooling stage and a heating stage. If the atoms are hot and the laser is tuned correctly, we will get more cooling than heating. Atoms that are not deep in the trap may gain enough energy to escape. To check whether if laser cooling has been successful, the best method is to ramp down the Ioffe trap and observe the timing of antihydrogen annihilations. It is possible to identify the difference between cooled and uncooled antihydrogen atoms by looking at the separation between loss peaks. But, this still hasn't been demonstrated experimentally with antihydrogen atoms.

The Lyman-alpha laser source, at the ATRAP experiment, is based on a pulsed Ti:sapphire laser system operating at 729 nm, whose frequency is stabilized with an optical frequency comb [30]. The 729 nm light is injected into an oscillator cavity that maintain the laser at high density. A pump laser gets injected into the oscillator cavity to produce high energetic pulses. Using a multi-pass amplifier, very high energy pulses are produced at a wavelength of 729 nm. The 729 nm source is frequency doubled in a LBO non-linear crystal that produces the 365 nm wavelength. Finally, the 729 nm light gets tripled in a Kr/Ar gas cell to produce Lyman-alpha radiation. There are two Lyman-alpha paths, the radial cooling path and the axial cooling path (Fig 2.12). After frequency conversion, the Lyman-alpha laser produces up to 5.7 μW of average power at the Lyman-alpha wavelength [30].

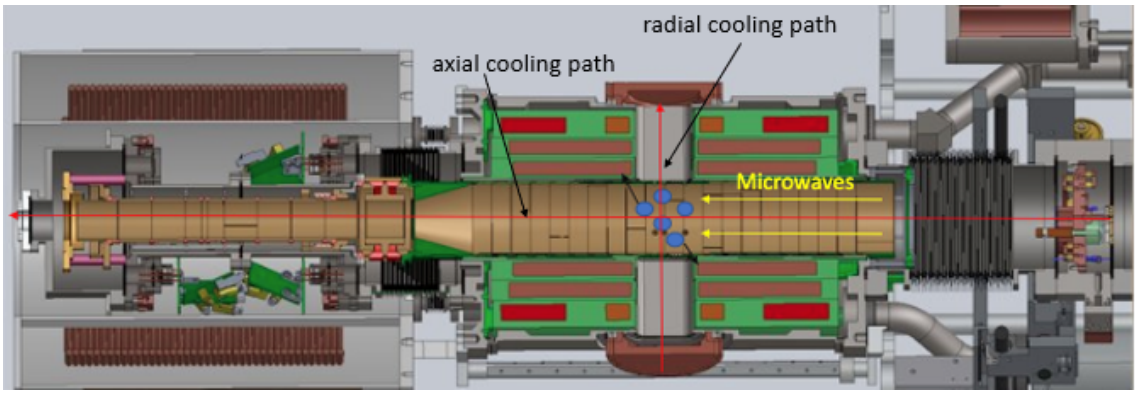

Figure 2.12: Lyman-alpha paths and microwaves.

Chapter 3

Antihydrogen production and plasma diagnostics

3.1 Introduction

Plasmas with a single sign of charge, such as antiprotons, electrons or positrons can be confined in a Penning trap. The Penning trap fills the role of a neutralizing species by confining positrons and antiprotons at the same time. These plasmas are called non-neutral because they are charged. They are plasmas because the Debye length $\lambda_D = \sqrt{\epsilon_0 k_B T/nq^2} \approx 10$ - 100 μm is small compared to the several mm dimension of particle clouds. Non-neutral plasmas can be confined for hours in Penning traps. In addition, they can be cooled to cryogenic temperatures.

Low temperatures are essential for antihydrogen production as only antihydrogen atoms at a temperature of 0.4 K or below can remain confined in the Ioffe octupole trap. Antihydrogen atoms are formed most rapidly by three-body recombination

which requires a high positron plasma density and low plasmas temperature. The temperature, the density and the geometry of plasmas are critical parameters for the antihydrogen production.

To characterize positron, electron and antiproton plasmas, several diagnostics have been implemented at the ATRAP experiment. With a plasma imaging system [24], we were able to image plasmas and to check whether if positrons and antiprotons are on the same axis and at the same size before the antihydrogen production. The plasma imaging is a destructive system for the particles: the plasma is sent on a phosphor screen where particles annihilate. Alternatively, a non-destructive measurement of plasma mode oscillations, defined later in this chapter, characterizes plasmas for large enough numbers of particles. This diagnostic can very quickly characterize positron and electron plasmas in a Penning trap.

3.2 Non-neutral plasmas at CERN

To produce trapped antihydrogen atoms, we use antiproton, positron and electron plasmas. Antiprotons come from a unique dedicated facility at CERN (the antiproton decelerator AD). Electrons and positrons are produced internally within the ATRAP experiment.

3.2.1 Electron and positron plasmas

We produce electrons at ATRAP, using a 248 nm excimer laser [31], sent through a centered 1.5 mm diameter hole, located on the XY translation stage (Fig 2.9). The hole is surrounded by Faraday cups that eject detectable electrons when the

excimer laser hits them rather than going through the hole. When the excimer laser goes through the hole, it hits a beryllium degrader located at the bottom of the electrode stack. Electrons are ejected from it and trapped in the Penning trap (Fig 2.8). Electrons are used to slow and cool antiprotons and positrons.

Positrons, at ATRAP, are emitted by a 50 mCi ^{22}Na source (Fig 3.1). They first pass through a frozen neon moderator and through a N_2 gas for resonant loss. Positrons are then captured and spun in a Penning-Malmberg trap with SF_6 gas, where they loose even more energy. Finally, they are pulsed at 60 eV from the accumulator to the apparatus and steered along a magnetic guide with 72 sets of magnets and approximately 130 DC coils. Positrons enter the apparatus from above (Fig 3.1). We typically load 1.5 million positrons every 30 seconds.

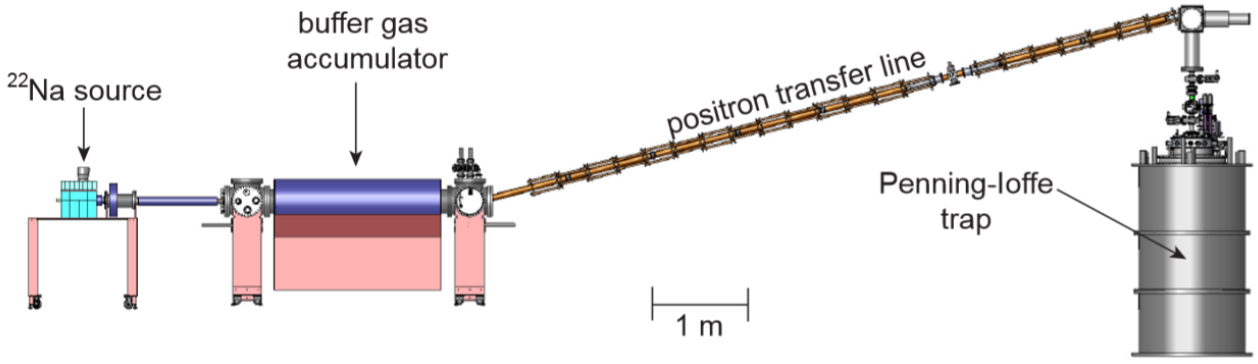

Figure 3.1: Accumulation of positrons [20].

To catch and cool positrons, we use a 4 mm radius electron plasma containing 150 million electrons [20]. We will explain in chapter 4 how electron plasmas with a certain radius and number of particles are formed. Positrons slow when they collide with the electron plasma, and are then caught into two negative wells (Fig 3.2). The electron plasma is then dumped out and the 2 positron clouds mix and form a single

potential well. We typically load 30 million positrons to start an antihydrogen trial.

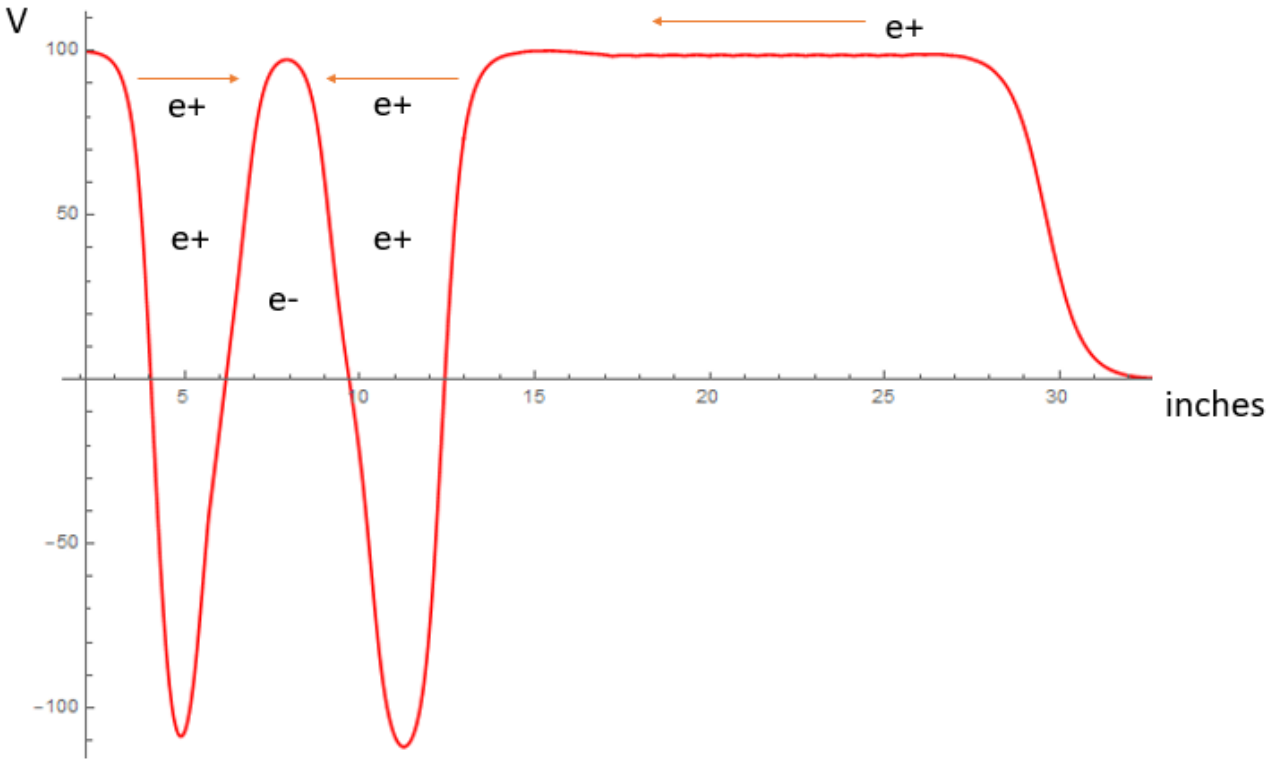

Figure 3.2: Potential well to catch positrons.

3.2.2 Antiproton plasmas

CERN produces and provides the antiprotons. A bottle of hydrogen gas is connected at one end of a linear accelerator called Linac 2. Protons enter into the linear accelerator [20] and reach an energy of 50 MeV. These protons are then injected into CERN's proton synchrotron (Fig 3.3) and are accelerated near the speed of light where they reach an energy at up to 25 GeV. Finally, protons collide with a dense iridium target, forming antiprotons by the reaction $p + p \rightarrow p + p + p + \bar{p}$.

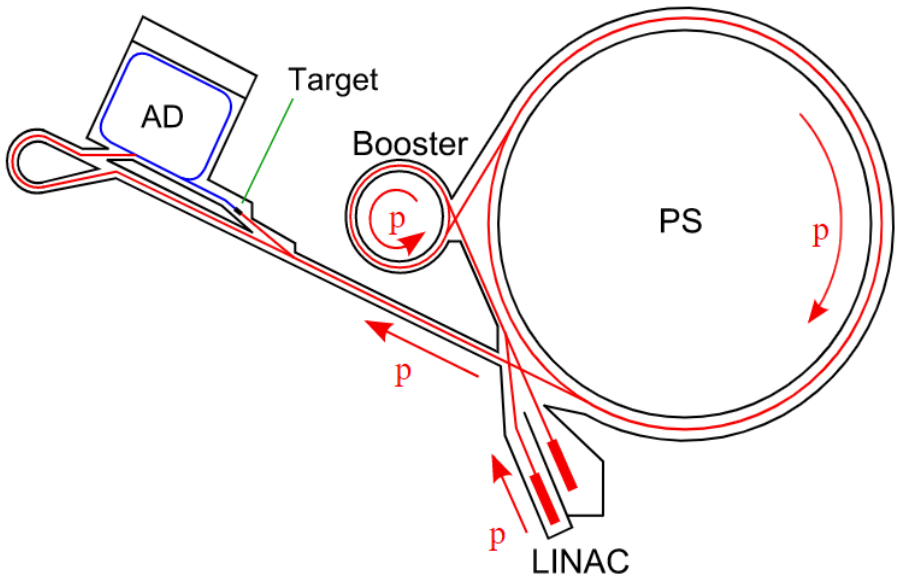

Figure 3.3: CERN facility.

Antiprotons emerging from the target are focused into an injection transport line by a magnetic horn. These $\bar{p}$ are collected, decelerated and cooled in the CERN Antiproton Decelerator (AD). The AD is a ring [32] composed of bending and focussing magnets that guides the antiprotons, while strong electric fields within RF cavities slow them down. The spread in energy of the antiprotons and their deviation from their track is reduced by a technique known as stochastic cooling [32]. The antiprotons are decelerated and merge also with a 20 mm diameter electron beam. The electron and antiproton velocities are matched and Coulomb collisions transfer the heat of the antiprotons to the electrons [32]. The AD delivers at the end antiprotons at 5 MeV energies to experiments in the AD hall. Approximately every 2 minutes, the AD delivers a 200 ns pulse of 3×10^7 $\bar{p}$ to one of the five experimental zones connected to the beamline [20].

The antiprotons enter the ATRAP apparatus from below. They pass through a

gas filled energy tuning cell, two 10 micrometers titanium foil windows, six layers of 6.4 micrometers aluminized mylar foil and a 100 micrometers beryllium degrader [20]. At the end, approximately, 1 out of 200 antiprotons have an energy of 5 keV or less. We loose many antiprotons via annihilation through this process going from 10^7 incident antiprotons to only 10^5 captured. We will explain in chapter 4 how antiprotons are caught in the Penning trap.

In the future [32], a new ring called ELENA (extra low energy antiprotons), will slow antiprotons from 5 MeV to 100 keV. Experiments will be able to trap 100 times more antiprotons per unit time for 24 hours per day using 50 times lower energy antiprotons. ELENA ring will further cool and deliver antiprotons to experiments through new electrostatic beam lines.

3.3 Physical processes involved in the antihydrogen production

When antiprotons and positrons mix together, most Rydberg antihydrogen atoms are formed by three-body recombination [33, 34]. Two positrons scatter near the antiproton,

$$\bar{p} + e^+ + e^+ \rightarrow \bar{H} + e^+.$$

One loses enough energy to become bound to the antiproton, while the other carries away the binding energy and conserves momentum. The recombination rate per antiproton [20],

$$\nu_{tbr} = (n_e \sigma_{tbr} v_e)(\frac{4}{3}\pi b_{min}^3 n_e), \tag{3.1}$$

is the classical collision rate of an antiproton within a positron plasma, multiplied by the probability that a second positron is located within the collision radius b_{min}. Here n_e represents the positron plasma density, v_e is the positron plasma velocity, $b_{min} = q^2/(4\pi\epsilon_0 k_B T)$ is the classical distance of closest approach, and σ_{tbr} is the three-body recombination cross section with $\sigma_{tbr} \approx b_{min}^2$. By approximation,

$$\nu_{tbr} \approx (n_e)^2 (T_e)^{-9/2}. \tag{3.2}$$

The rate of antihydrogen formation depends very strongly on the positron plasma temperature and density. Three-body recombination occurs rapidly when the positron plasma density is high and the positron plasma temperature is low. The positron plasma density is inversely proportional to the plasma radius squared. For this reason, plasmas are compressed to small radii, as will be described.

Other processes contribute to antihydrogen production but at a much lower rate. For radiative recombination, a photon carries away the excess energy required to form a bound state

$$\bar{p} + e^+ \rightarrow \bar{H}(n) + \gamma.$$

However, the production rate per antiproton is many orders of magnitude more efficient for TBR than for radiative recombination [20].

Finally, the last process known for the antihydrogen production is laser-controlled charge-exchange demonstrated by ATRAP [35]. Charge-exchange (Fig 3.4) involves the collision between a Rydberg positronium (Ps), a highly excited bound state of an electron and a positron, with an antiproton. After cesium atoms emitted from an oven are excited to Rydberg states $Cs + h\nu \rightarrow Cs^*$ by application of the 852 nm and the 511 nm laser light, they pass through and charge-exchange with a positron plasma

$Cs^* + e^+ \rightarrow Ps^* + Cs^+$. A second charge-exchange between Rydberg positronium and an antiproton plasma forms Rydberg antihydrogen atoms $Ps^* + \bar{p} \rightarrow \bar{H}^* + e^-$. Charge-exchange is the only alternative to three-body recombination demonstrated to form $\bar{H}$ atoms in a nested Penning-Ioffe trap. However, the production rate per antiproton is many orders of magnitude more efficient for TBR than for double charge-exchange [36].

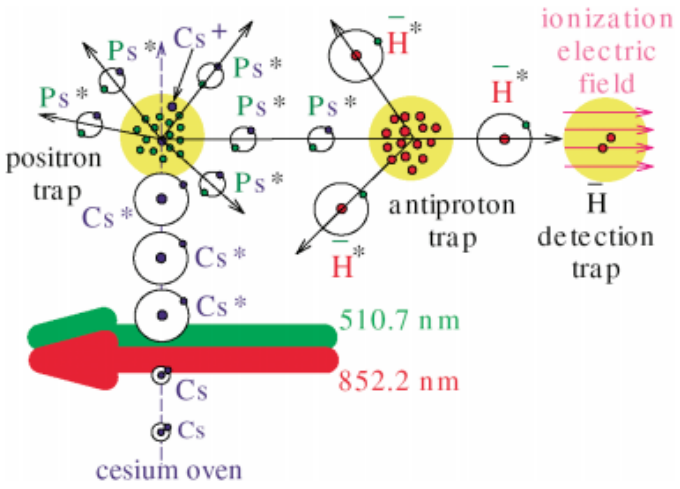

Figure 3.4: Laser-controlled charge-exchange process [37].

3.4 Non-neutral plasmas characteristics and antihydrogen production

For three-body recombination, we can deduce a certain set of plasma parameters to produce efficiently trapped antihydrogen atoms. Just before mixing antiprotons and positrons, plasmas should be on the same axis and at the same size (Fig 3.5). We would like to achieve a good overlap between the antiproton cloud and the positron

plasma during the mixing sequence. In addition, plasmas radii should be as small as possible and plasmas temperature should be as low as possible (Fig 3.5). If we consider that the antiproton plasma has a temperature of 3.5 K, the smallest antiproton plasma temperature ever measured in our Penning trap [21], we can determine the percentage of antiprotons at a temperature of $T_o = 0.405$ K (Ioffe octupole trap depth) or below using a Boltzmann distribution

$$P(T_o) = (\frac{m_p}{2\pi k_b T_{\bar{p}}})^{3/2} \int_{T=0}^{T=0.405} e^{\frac{-m_p}{2k_b T_{\bar{p}}} V_{\bar{p}}^2} d^3\vec{v}. \tag{3.3}$$

We would like to integrate over the maximal antiprotons trappable velocity. The maximal potential energy is equal to $k_b T_o$=$0.5 m V_{\bar{p}}^2$. As a consequence, the maximal antiprotons trappable velocity is 83.5 m/s in the Ioffe octupole trap. This is the maximum velocity a $\bar{H}$ atom can travel at the point of interest without its kinetic energy exceed the trap depth.

$$P(V_{\bar{p}}) = 4\pi(\frac{m_p}{2\pi k_b T_{\bar{p}}})^{3/2} \int_{V_{\bar{p}}=0}^{V_{\bar{p}}=83.5} V_{\bar{p}}^2 e^{\frac{-m_p}{2k_b T_{\bar{p}}} V_{\bar{p}}^2} \, \mathrm{dV_{\bar{p}}} \approx 2.8\%. \tag{3.4}$$

Only 2.8% of $\bar{p}$ will have a temperature less than 405 mK. In general, we can form more antihydrogen atoms with more antiprotons. However, it is harder to compress and reduce the temperature of a plasma with more particles. At ATRAP, we use approximately 360 000 antiprotons for the antihydrogen production. Finally, during a trial, we load more positrons than antiprotons, so all antiprotons have a chance to participate in three-body recombination. For a spherical plasma, if we assume that ρ_{e+}=1 mm (best typical positron plasma radius), $(n_0)_{e+} = 6.5 \times 10^{13}\ m^{-3}$, B=1 T and z_p=10 mm (typical half-lengh of a plasma in our Penning trap), we have

$$N_{e+} = \frac{4}{3}\pi \rho_{e+}^2 z_p n_0 \approx 3000000. \tag{3.5}$$

To sum up, to make efficiently trapped antihydrogen atoms in our apparatus, plasmas should be on the same axis, at the same size, at the smallest radii and the lowest temperature possible. About 360 000 antiprotons and 3 million positrons for the antihydrogen production seems optimum.

3.5 Plasmas diagnostics

Several diagnostics to characterize plasmas have been implemented at the ATRAP experiment. With the plasma imaging system [24], we can check wether if positrons and antiprotons are on the same axis and at the same size before the mixing sequence (Fig 3.5). Alternatively, the plasma modes system, improved in 2018, characterizes quickly positron and electron plasmas with a minimum of 2 million particles. With this diagnostic, we can determine the plasma radius, the plasma density and the plasma half-length. The ATRAP experiment also successfully implemented a diagnostic [20] to measure the antiproton plasma temperature in the past (Fig 3.5). The measurement of the antiproton plasma temperature, to efficiently produce trapped antihydrogen atoms, is essential. In fact, antiprotons can be heated, without cooling mechanism, to several hundreds of Kelvin due to high voltage pulses applied in the trap. Finally, using scintillating detectors or a faraday cup, we can count the number of positrons, electrons or antiprotons in the electrode stack (Fig 3.5).

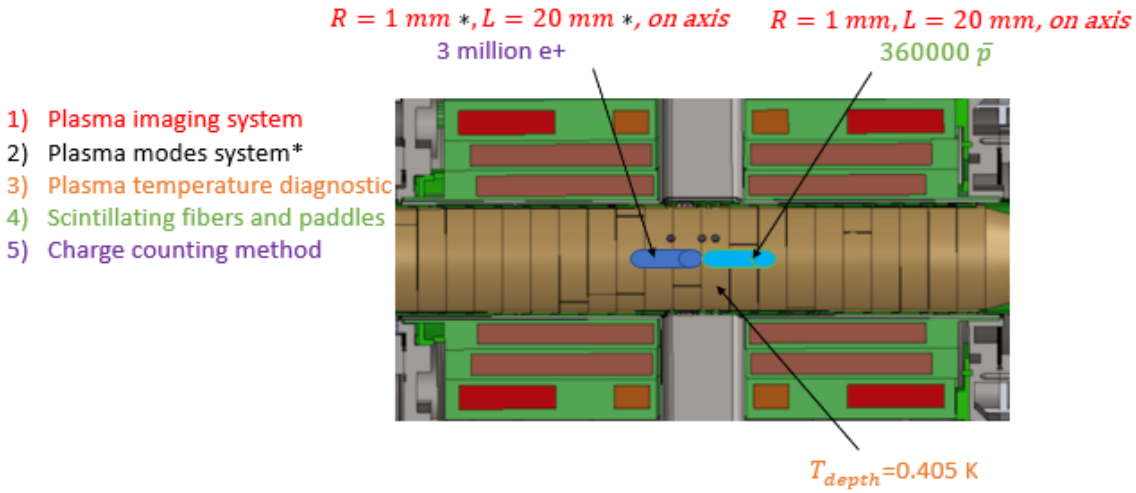

Figure 3.5: Plasmas diagnostics and plasmas parameters for the antihydrogen production at ATRAP.

3.5.1 Plasma modes system

The plasma modes system characterizes quickly non-neutral plasmas in the Penning trap. Within a plasma, particles behave collectively with N particles and N normal modes. In particular, 2 plasma modes fully characterize an electron or a positron plasma, the center-of-mass mode ω_z and the quadrupole mode ω_2 [38]. The center-of-mass mode is an harmonic oscillation of the plasma (Fig 2.2). The quadrupole mode is an oscillation in the length and radius of a spheroid whose axis of symmetry is oriented along the z direction (Fig 3.6).

In 2017, we were able to detect plasma modes, for a positron or an electron plasma, in the lower electrode stack, with a minimum of 20 million particles. However, we were not able to detect plasmas modes in the upper electrode stack, where electrodes are twice bigger in diameter. To make efficiently trapped antihydrogen atoms, we would like to characterize plasmas for a smaller number of particles. In addition,

we would like to detect plasma modes in the upper electrode stack (where trapped antihydrogen atoms are formed).

In order to improve the sensitivity, we would like to compare the force applied on plasmas, when exciting their modes, between the upper electrode stack and the lower electrode stack. We consider that one electrode generates RF frequencies, an other electrode holds the plasma and the last electrode receives the voltage signal from plasma oscillations (Fig 3.6). We use the following expansion of the electric potential [39]

$$\phi(r,\theta) = \frac{Vo}{2}\sum_{j=0}^{\infty} Cj(\frac{r}{d})^j Pj(cos(\theta)). \tag{3.6}$$

C_j is the coefficient for a cylindrical electrode of half-length z_0 and radius ρ_0

$$Cj = \frac{2}{Vo}\frac{(-1)^{j/2}}{j!}\sum_{n=0}^{\infty} A_n(k_n d)^j. \tag{3.7}$$

To find the potential along the positive z-axis, we set $cos(\theta) \approx 1$, r=z.

$$\phi(z) = \frac{Vo}{2}\sum_{j=0}^{\infty} Cj(\frac{z}{d})^j. \tag{3.8}$$

As a consequence, the force applied on a plasma is

$$\frac{d\phi(z)}{dz} = \sum_{j=0}^{\infty}\sum_{n=0}^{\infty}\frac{(-1)^{j/2}}{j!}A_n(k_n d)^j\frac{d}{dz}(\frac{z}{d})^j. \tag{3.9}$$

The ratio of forces applied on plasmas between the lower electrode stack, where ρ_0=18 mm, and the upper electrode stack, where ρ_0=34 mm is 1.7. The force applied on a plasma is almost reduced by a factor of 2 in the upper electrode stack so the detection of particles will be reduced by a factor of 4, for the same applied potentials. To detect plasma modes in the upper electrode stack, we would need, as a consequence, to improve the sensitivity.

The current plasma modes system excites mode oscillations, with a 30 to 60 MHz drive, from a frequency synthesizer. The frequencies are sent within 1 μs using a rf switch (Mini-circuits ZYSWA-2-50DR). When the plasma motion is excited, it induces current oscillations on the opposite trap electrode, which generates a voltage across a resistor (Fig 3.6).

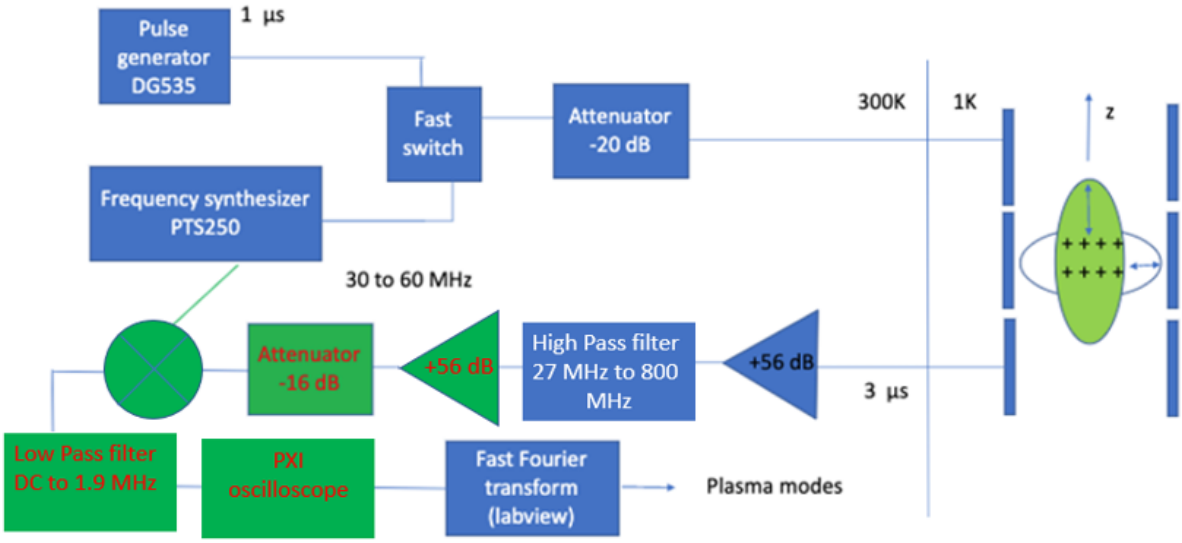

Figure 3.6: New plasma modes system (elements from the new plasma modes system are represented in green).

We wait 3 μs after the application of the drive frequency before observing induced oscillations on the electrode. The signal is amplified at room temperature (Fig 3.6) and sent to a high pass filter. The signal goes through an other amplifier and finally into a mixer, via a 16 dB attenuator (Fig 3.6). The signal coming from the trap, is mixed with a frequency synthesizer signal, which has the same frequency as the drive frequency. The mixer substrates the absolute value between the 2 frequencies and the resulting signal goes through a low pass filter (Fig 3.6). Finally, an oscilloscope (PXI

5922) provides a resolution at up to 24 bits with a sample rate at up to 15 MS/s. The old scope (tektronix RM2000 rack mount), used in the past for the plasma modes system, had a sample rates of 2 GS/s and a resolution of only 8 bits. With the new oscilloscope, the signal is fast fourier transformed to determine plasma mode frequencies. Oscillations are visible for typically 100 μs before damping away. The average of repeated measurements gives a result at the several-hundred Hz accuracy level.

Due to these improvements, we were able to get more precision on voltage data, so the fourier transform was better able to separate out the signal components. In the lower electrode stack, we were able to detect plasma modes for 2 million particles instead of 20 million particles. In the upper electrode stack, we were able to detect plasma modes for a minimum of 10 million particles. The sensitivity has been improved by a factor of 10.

3.5.2 Determination of plasma characteristics with plasma modes

The geometry for a real plasma in a cylindrical trap deviates from a spheroid. For simplify, we assume that the plasma has a spheroidal shape. The mode frequencies for spheroidal plasmas, in ideal Penning traps, have been calculated in the T $\rightarrow$ 0 limit [40]. A mode frequency ω_l is related to the plasma frequency ω_p and the aspect

ratio α through the following equation

$$\frac{(\omega_p)^2}{(\omega_l)^2} = 1 - \frac{k_2}{k_1}\frac{P_l(k_1)Q_l'(k_2)}{P_l'(k_1)Q_l(k_2)}. \tag{3.10}$$

Q_1^0 is the associated Legendre function of the second kind, the plasma frequency ω_p corresponds to the typical oscillation frequency in response to the displacement of a small charge in the plasma with $(\omega_p)^2 = 2\omega_r(\omega_c - \omega_r)$. Finally, the ratio of the constants k_2 and k_1 has the following expression

$$\frac{k_2}{k_1} = \frac{(\alpha^2 - 1 + \frac{(\omega_p)^2}{(\omega_l)^2})^{0.5}}{(\alpha^2 - 1)^{0.5}}. \tag{3.11}$$

Similarly, if we consider the plasma as a spheroid, the center-of-mass mode is defined as [41]

$$\frac{(\omega_z)^2}{(\omega_p)^2} = \frac{Q_1^0(\frac{\alpha}{(\alpha^2-1)^{0.5}})}{\alpha^2 - 1} = f_p(sol). \tag{3.12}$$

The COM frequency is $f_z = \frac{\omega_z}{2\pi}$ and the quadrupole frequency is $f_2 = \frac{\omega_2}{2\pi}$. Taking into account the ratio of constants $\frac{k_2}{k_1}$ and the definition of $\frac{(\omega_p)^2}{(\omega_l)^2}$, we get the following expression to find the root of the aspect ratio α_{sol}

$$0 = ((\alpha_{sol})^2 - 1)(1 - (\frac{k_2}{k_1})^2) + \frac{(\omega_p)^2}{(\omega_l)^2}. \tag{3.13}$$

With α_{sol}, $f_p(sol)$, the number of particles N and plasma modes (ω_z ; ω_2), we can determine the plasma density $n_0 = \frac{(2\pi f_p(sol))^2 \epsilon_0 m_e}{(q_e)^2}$, the plasma radius $\rho_p = 100(\frac{3N}{4\pi\alpha_{sol} n_0})^{1/3}$ and the plasma half-length $z_p = \alpha_{sol}\rho_p$. If $\alpha < 1$, the plasma has an oblate shape. If $\alpha > 1$, the plasma has a prolate shape.

As an example, for a plasma with 21 million positrons, compressed in the lower electrode stack with a rotating electric field for 300 s, the center-of-mass frequency is 34.5 MHz and the quadrupole frequency is 56.2 MHz. As a result, the plasma density

is $n_0 = 2.8 \times 10^9 cm^3$, the plasma axial half-length is $z_p = 9.8$ mm, the plasma radius is $\rho_p = 0.43$ mm and the plasma aspect ratio is $\alpha = \frac{z_p}{\rho_p} = 23.2$. The plasma has a prolate shape.

3.5.3 Plasma imaging system

The plasma imaging system was fully implemented at the ATRAP experiment in 2018 [24]. For the first time, we were able to image electron, positron and antiproton plasmas. With this diagnostic, we can especially measure the antiproton plasma radius. In fact, we cannot characterize an antiproton plasma with the plasma modes system, due to the limited number of particles. To check wether if plasmas are in the best conditions for the antihydrogen production, we image positron and antiproton plasmas, just before the mixing sequence, when the Ioffe octupole trap is at full current. In the ideal case, plasmas should be on the same axis and at the same size.

To image plasmas, we use 2 micro-channel plates and a phosphor screen located on the XY translation stage (Fig 3.7). To send particles onto the phosphor screen, the XY stage moves to centre the plasma imaging assembly at the center of the trap.

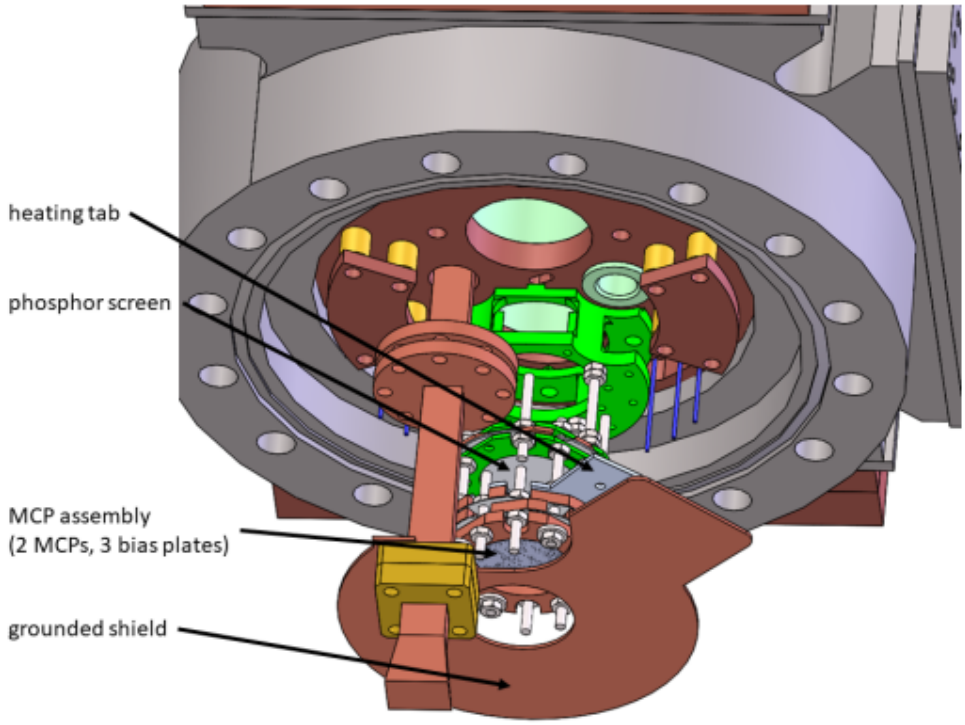

Figure 3.7: Phosphor screen-MCPs assembly [24].

Two 25 mm diameter micro-channel plates (MCPs) amplify the number of electrons received from a plasma. During normal operation, the bottom bias plate (the MCP face viewing the particles) is at +100 V, the middle plate (the back of the first MCP and front of the second) is at + 1 kV, the top plate (the back of the second MCP) is at +2 kV, and the phosphor screen is at +3 kV (Fig 3.8). The MCP's back plate voltage relative to the front can control the gain of the MCP and is chosen to avoid saturation.

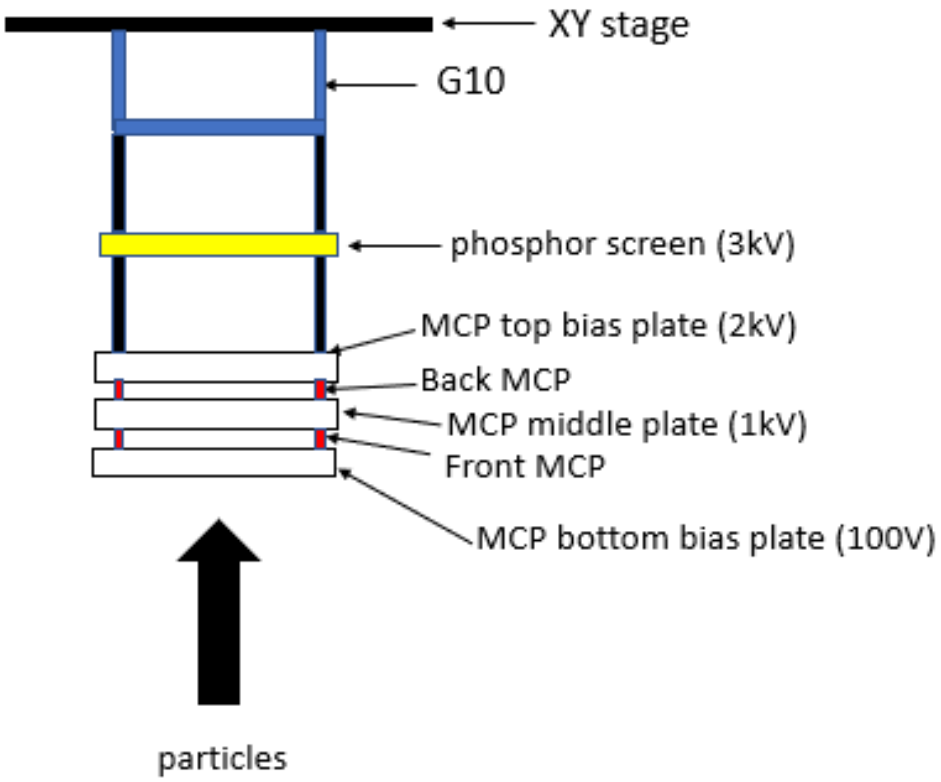

Figure 3.8: Micro-channel plates.

Antiprotons annihilate when striking the MCP. The high energy secondary particles that result from the annihilation can excite additional cascades, enhancing the MCP gain. We can easily image plasmas with 360 000 antiprotons. A heating tab (Fig 3.7) is also used to warm up MCPs and to make sure surfaces have electrical charges. We usually heat the MCPs for 1 min to 20 K, after each diagnostic, using a 1 W diode laser. The electron shower produced by a MCP is accelerated onto the phosphor screen.

The phosphor screen (P22 phosphor from Kimball Physics) converts electrons into photons at an average of 120 photons/e- when it is biased at 3 kV. The 20 mm diameter phosphor screen (Fig 3.7) emits light over a broad spectrum at an average

wavelength of 550 nm. It has a typical decay time of 4 ms. Finally, a ground shield (Fig 3.7) is used to avoid building up charge from pulsing particles.

To take a picture of the emitted photons from the phosphor screen, we use a camera connected to a cube above the apparatus (Fig 3.9). The camera is located 1.5 m away from the phosphor screen. An optics holder is mounted inside the cube to focuse the camera onto the phosphor screen.

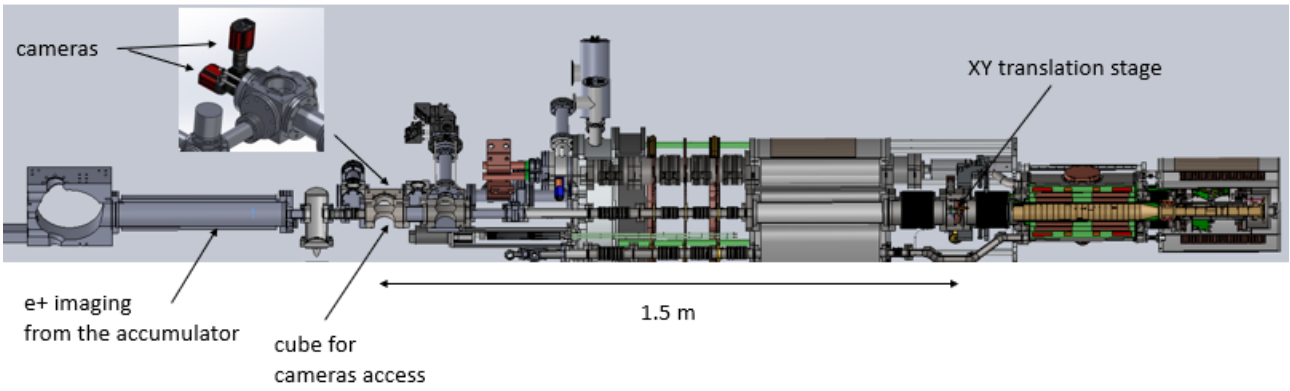

Figure 3.9: Camera imaging system.

This optics holder is also used to send the Lyman-alpha laser into the trap, to image positrons arriving from the positron accumulator or send the 1 W diode laser onto the heating tab (Fig 3.9). We use a linear translation stage to move the optics holder. An other camera images positrons arriving from the positron accumulator (Fig 3.9).

To send a plasma onto the phosphor screen (Fig 3.10), the plasma is initially trapped into the electrode stack, on a positive well when using positive charged particles, or on a negative well when using negative charged particles. A DEI positive or negative high voltage pulser pulses the plasma onto the phosphor/MCPs assembly. We send a fast pulse of $\pm$ 250 V for 4 μs (Fig 3.10). To send positrons towards

the XY translation stage, we apply a negative voltage ramp on the left hand side of the plasma and a positive voltage ramp on the right hand side (Fig 3.10). On the contrary, to image electrons or antiprotons, a positive voltage ramp is applied on the left hand side of the plasma and a negative voltage ramp is applied on the right hand side of the plasma. Once the DEI high voltage pulser sends the pulse, the camera is triggered.

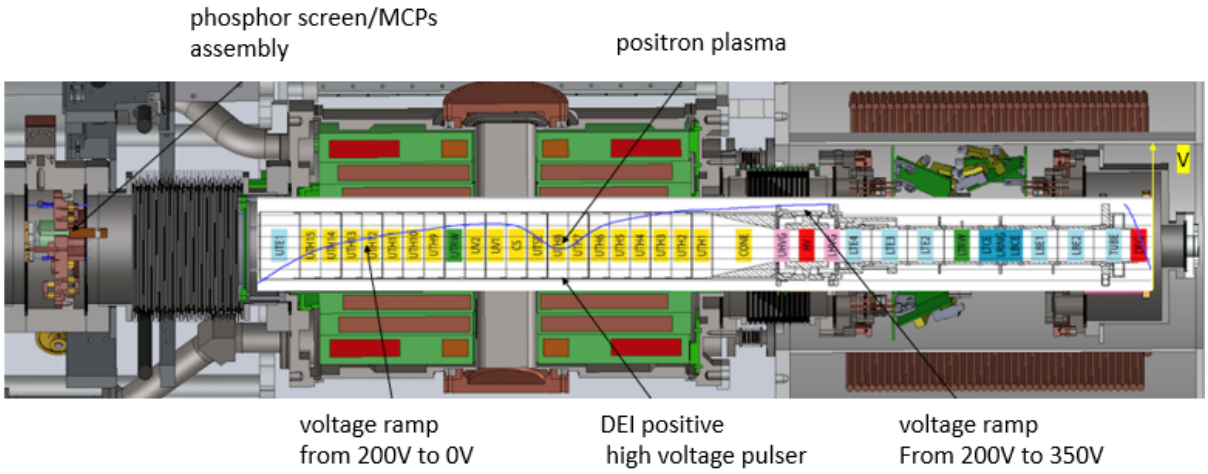

Figure 3.10: Plasma imaging system.

3.5.4 Plasma imaging results

We imaged the positron and the antiproton plasmas, just before the mixing sequence, when the Ioffe octupole trap is at full current [24]. The best antiproton plasma that we were able to image, before mixing particles, has a 4 mm radius with 360 000 antiprotons (Fig 3.11). The best positron plasma that we were able to image, before mixing particles, has a 1 mm radius with 20 million positrons (Fig 3.11). We also imaged a 0.5 mm radius electron plasma, from the lower electrode stack, at a 1 T field, with 30 million electrons (Fig 3.11). To measure plasmas radii, we use a

gaussian fit and an ellipsoidal fit along the centerline. The color scale of the following plasmas pictures represents the pixel brightness.

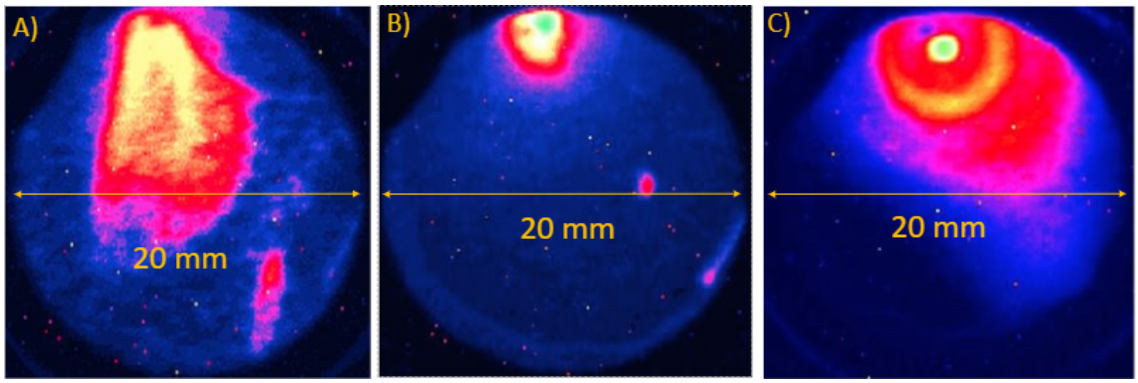

Figure 3.11: A) 4 mm radius antiproton plasma with 360 000 particles. B) 1 mm radius positron plasma with 20 million particles. C) 0.5 mm electron plasma with 30 million particles. The diameter of the phosphor screen is 20 mm.

By repeating the exact same procedure to form the positron plasma represented above, the positron plasma reveals a 34.2 MHz center-of-mass frequency and a 54 Mhz quadrupole frequency, with a density of 5.1×10^8 cm^{-3}. Using the approximation of a spheroidal plasma, the positron plasma radius is 1 mm and confirmes the result from the plasma imaging system.

If we superpose the 3 previous plasmas represented above, positron, electron and antiproton plasmas seem to be almost on the same axis (Fig 3.12). Particles follow magnetic field lines closely as they are constrained transversely by cyclotron motion. However, lightest particles such as electrons or positrons follow field lines more closely due to their cyclotron motions. An electron is more tighly bound to the field line due to his mass. The phosphor screen on the XY translation stage is located at a field comprised between B=0.3 T and B=0.6 T.

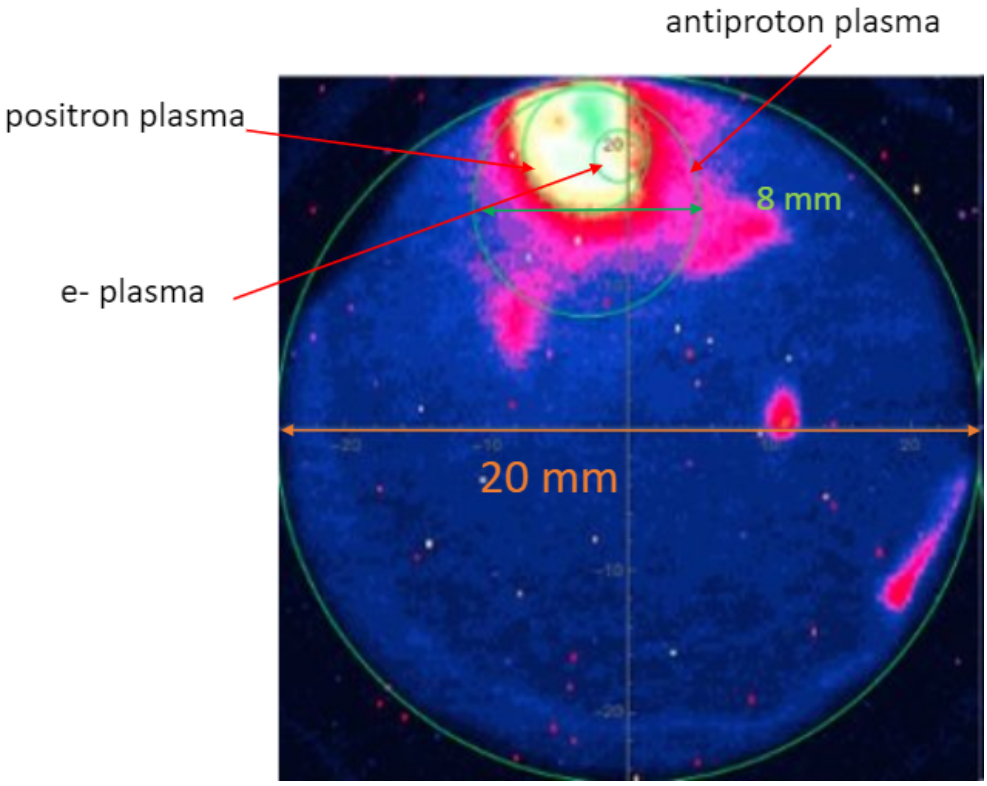

Figure 3.12: Superposition of plasmas represented in Fig 3.11.

To image plasmas from the lower electrode stack, when the field boosting solenoid is at full current, particles are initially trapped in a 3.7 T magnetic field. When particles travel through the trap, magnetic field lines diverge and the size of particles orbits increase. The radius of the plasma changes as $r_{trap} = r_{MCP}\sqrt{B_{MCP}/B_{trap}}$, where r_{trap} is the radius of the plasma in the trap region when the magnetic field is B_{trap}, and r_{MCP} is the radius of the plasma in the MCP region when the magnetic field is B_{MCP}.

With the plasma imaging system, we can determine if plasmas expand, after a certain amount of time, when the Ioffe octupole trap is at full current. We imaged the positron plasma with 20 million particles, just after the octupole trap was ramped

up, and 10 min after (Fig 3.13). The positron plasma was initially located at the Ioffe trap minimum. After 10 min, the positron plasma expanded from 1 mm to 2 mm radius (Fig 3.13B).

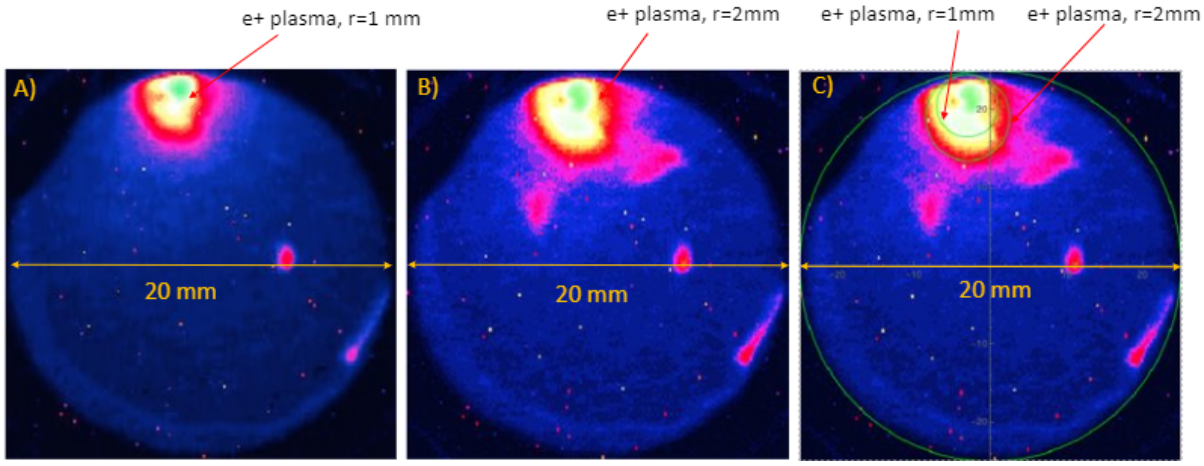

Figure 3.13: Expansion of the positron plasma in the Ioffe octupole trap. A) Ioffe octupole trap at full current for few seconds. B) Ioffe octupole trap at full current for 10 min. C) superposition of the 2 previous plasmas.

In a real trial, the positron plasma is confined less than 1 min at the Ioffe trap minimum before mixing particles. It seems that the positron plasma does not really expand in the Ioffe octupole trap, which is essential for the antihydrogen production.

3.5.5 Number of charged particles in the electrode stack

To produce trapped antihydrogen atoms, it is fundamental to know how many positrons, electrons and antiprotons are trapped in the electrode stack. To count the number of electrons, we use a negative low voltage pulser, called saturated switch, connected to an electrode. Low voltage pulses eject particles slowly on a faraday cup, connected to the degrader. When charged particles hit the faraday cup, a voltage signal is extracted across a capacitor and amplified to extract the charge deposited

(Fig 3.14). The number of particles is obtained via the following relation

$$V = -\frac{Nq}{2C_{eff}}, \tag{3.14}$$

with C_{eff} the effective capacitance [20]. The result is displayed on a scope. To count the number of positrons, we use a DEI positive high voltage pulser instead of a saturated switch.

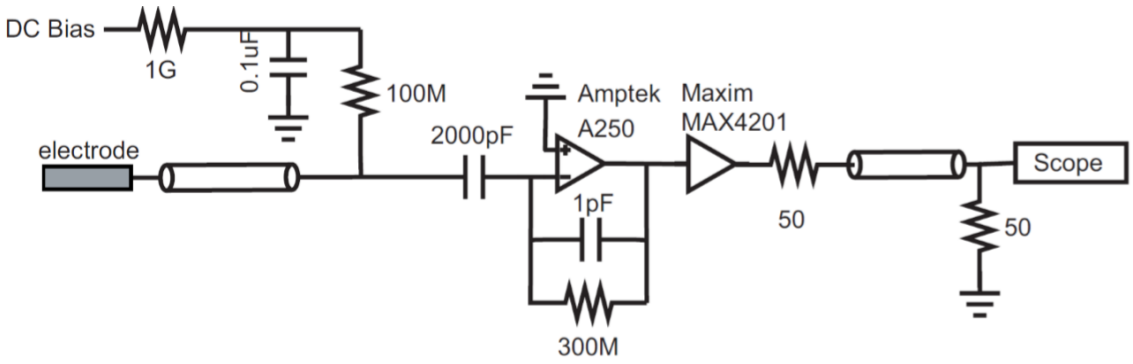

Figure 3.14: Method to count the number of positrons and electrons [20].

However, to count the number of antiprotons, the previous method cannot be used, because there are not enough antiprotons to produce a voltage signal above background with a faraday cup. Instead, we use detectors with scintillating fibers and paddles.

By reducing slowly the well depth of the antiproton cloud in the trap, antiprotons annihilate onto the electrodes wall and high energy pions are produced. After high energy pions hit scintillating fibers and paddles, photomultiplier tubes PMTs convert light into electrical signals. These electrical signals are sent to discriminators that extract a voltage signal above a certain background. Finally, signals are transferred to logic modules and then to a multi-channel scalar called MCS. The MCS acquires

the number of annihilations counts. A HSADC high speed analog to digital converter compares the timebase of the MCS and the voltage ramp.

3.5.6 Antiproton plasma temperature diagnostic

Before mixing particles, to form trapped antihydrogen atoms, it is essential to cool positron and antiproton plasmas to very low temperatures. We will see in chapter 4 methods to cool plasmas in the Penning trap. However, we expect that positrons cool very quickly to low temperatures in the electrode stack due to synchroton radiation, due to the 10^{-17} Torr vacuum into the experiment space and due to the 1 K pot. In fact, the synchrotron cooling time is

$$\tau_s = \frac{3\pi\epsilon_0 m^3 c^3}{q^4 (B_0)^2}. \tag{3.15}$$

A positron plasma in a 3.7 T magnetic field has a damping time of 0.19 s. However, the antiproton plasma has a damping time of 37 years.

A diagnostic has been implemented in 2012 to measure the antiproton plasma temperature [20]. Determination of the antiproton plasma temperature is achieved through the measurement of the antiproton evaporation rate as their confining well is reduced. A correction is made with a particle-in-cell plasma simulation due to the finite plasma self-potential. In fact, in a Penning trap, in addition to the trap external potential, the plasma induces a self-potential. For a plasma in a cylindrically symmetric trap, the motion of particles is represented by the following hamiltonian

$$H = \sum_{j=1}^{N} \frac{m v_j^2}{2} + q\phi(\vec{r_j}) \tag{3.16}$$

with $\phi(\vec{r}) = \phi_T(\vec{r}) + \phi_P(\vec{r})$=trap potential+plasma self potential. Taking into account the Penning trap external potential, with a relaxation program, we can determine the potential well with the plasma.

We directly probe the temperature distribution of the antiproton plasma by counting the number of antiproton that escape over a potential barrier of known height. The evaporation rate has to be slow but large enough to not interact with evaporative cooling (explained in chapter 4).

As an example, an antiproton plasma with 500 000 antiprotons, at a 4 mm radius, is hold for 600 s, in a 3.7 T field, with approximately 900 remaining electrons. We reduce the well depth of the plasma until antiprotons leak out. We ramp down the voltage of the antiproton plasma to 50 V. Then, we wait for equilibrium. Finally, the voltage is reduced to 10 V and we dump out the antiproton cloud by decreasing the voltage from 10 V to -50 V in 5 s. We get the following result

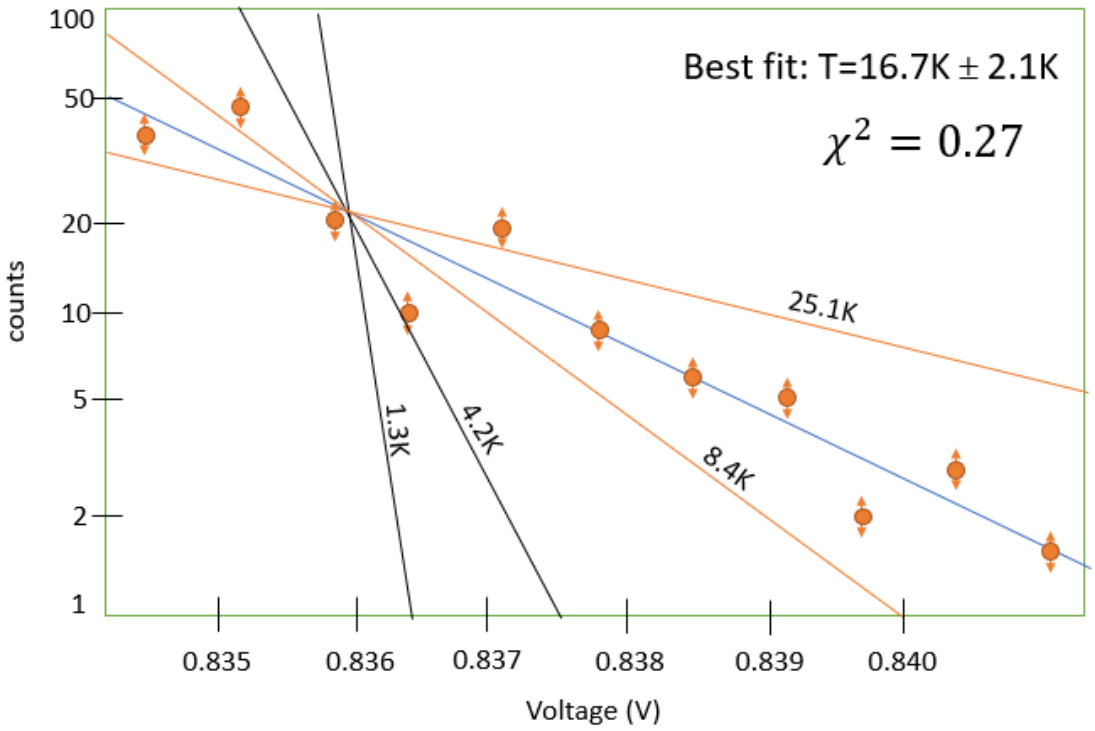

Figure 3.15: Number of counts versus voltage for an antiproton plasma in the trap.

To extract the temperature of the antiproton plasma, the first 0.1 % particles that escape are analyzed (Fig 3.15). We measure the slope m_0 of the curve of fitted line $-1/k_bT$ and find the temperature via the following relation

$$T = \frac{1}{m_0 k_b}\alpha, \tag{3.17}$$

with α the correction for the plasma self-potential, which is dependent on the plasma radius. In this example, the antiproton plasma temperature is around 17 K (Fig 3.15). The χ^2 of the linear fit is small because the points lie close to the line. The model seems to be valid.

Antiprotons cool very quickly at high field (3.7 T) with embedded electrons. This cooling method is called antiprotons cooling with embedded electrons. The cooling

rate of $\bar{p}$ with electrons is proportional to $(B_0)^2$. In the 3.7 T field, antiprotons cool from 1000 K to 31 K $\approx$ 600 s [20]. Then, the adiabatic cooling method, described in the next chapter, is used before the mixing sequence, to cool the plasma to 3.5 K [21]. However, in the 1 T field, to cool antiprotons from 1000 K to 31 K, it takes more than 1 hour. The cooling efficiency depends on the time for which the particles are allowed to interact, the number of electrons, and the radial overlap between the antiprotons and electrons.

We will see in the next chapter that plasma diagnostics are essential to improve plasmas manipulation techniques. With the plasma imaging system and a better plasma modes system, we can characterize plasmas quickly and more precisely than before to produce trapped antihydrogen atoms.

Chapter 4

Plasmas manipulation techniques and antihydrogen trials

At the ATRAP experiment, several plasmas manipulation techniques are used to prepare positron, electron and antiproton plasmas in the best conditions for the antihydrogen production. Plasmas at small radii, low temperatures and fixed densities are formed during each trial. The reproducibility of plasmas is possible due to the strong-drive regime-evaporative cooling method, described in this chapter [25]. By improving plasma diagnostics, we also improved plasmas manipulation techniques. About 5 trapped antihydrogen atoms per trial were produced using an hour long procedure [24].

4.1 Plasmas manipulation techniques

4.1.1 Antiprotons steering

To load as many antiprotons as possible on the axis with our trap electrodes (Fig 3.3), we steer AD magnets before starting an antihydrogen trial. This process consists of changing several AD magnets current values to make sure antiprotons enter into the trap on axis. The magnetic configuration of the AD is changing very frequently due to the AD magnets themselves and the number of experiments using superconducting magnets in the AD hall.

For this purpose, two detectors are mainly used: a PPAC (parallel plate avalanche counter) and a silicon detector. The PPAC [20] is mounted underneath the entrance to the Penning trap and is made of two sets of anode-cathode electrode pairs oriented perpendicularly to the beam path and to each other. Each anode has five independent aluminum strip electrodes. A voltage of 150 V is applied to the X and Y strips of the PPAC to attract the liberated electrons. The number of charges collected on each strip is proportional to the number of antiprotons. A voltage signal from each strip is extracted and displayed on an oscilloscope (Fig 4.1b). For a well-steered beam, the signals observed in the central channels of the silicon detector and PPAC should be maximized (Fig 4.1).

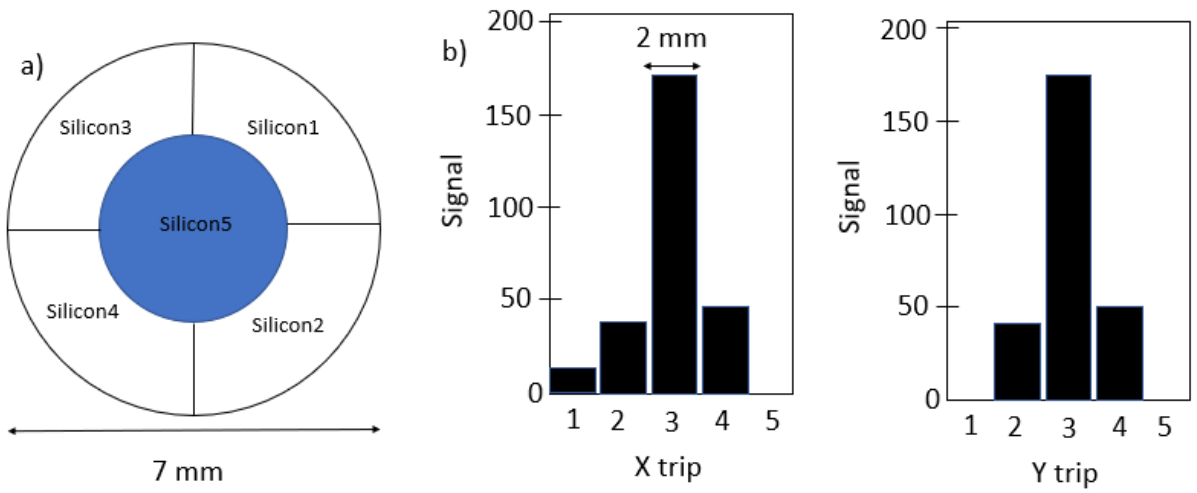

Figure 4.1: Silicon and PPAC display.

To make sure antiprotons enter into the electrode stack on axis, a segmented silicon detector is also placed where antiproton are ejected from the CERN beamline. A 7 mm diameter silicon detector is mounted on a rotatable feedthrough so that antiprotons can either hit the silicon detector or enter into the trap (Fig 4.1a).

4.1.2 Rotating wall and strong-drive regime-evaporative cooling method

To catch and cool antiprotons, an electron plasma with a large radius (6 mm) and a known number of particles helps. In order to form a large electron plasma radius, we use the rotating wall method. The electrode stack has 2 rotating wall electrodes. One rotating wall is located in the lower electrode stack and the other one is located in the upper electrode stack (Fig 2.4). In 2018, we couldn't use the upper rotating wall due to a short between electrodes.

The rotating wall electrodes are split into 4 quadrants and voltages,

$$V = V_0 cos(\omega_{RW} t - \pi j/2), \tag{4.1}$$

for j=(0,1,2,3), are applied to each of the quadrants respectively, with ω_{RW} the frequency. The amplitude varies between 1 Vpp and 9 Vpp. The time-varying rotating electric field compresses or expands the plasma. Any electric field rotating faster than the plasma in the same direction will exert a positive torque, resulting in radial compression. The plasma expands when the electric field rotates in the opposite direction.

We can either generate a dipole field or a quadrupole field (Fig 4.2). The quadrupole field stretches the plasma one way and then another with no rotation. However, if the plasma is already rotating, it will exert some torque. The dipole field exerts more torque because the gradient is stronger at the center of the plasma.

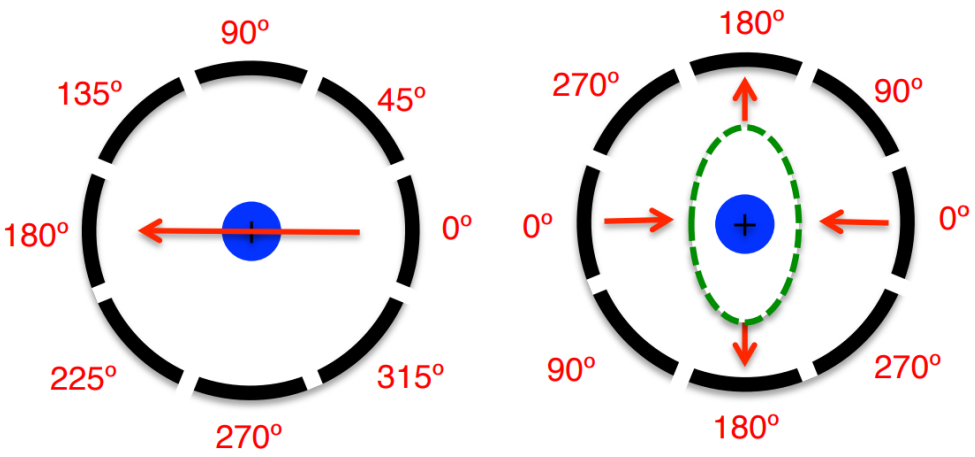

Figure 4.2: Dipole field and quadrupole field [42].

There are several ways to compress plasmas. We can excite the Trivelpiece-Gould (TG) modes using weak drives. TG modes are surface waves in a plasma that rotate

in the azimuthal direction. The angular momentum associated with the wave can be transferred to the bulk of the plasma. If the rotating wall continuously excites TG modes, a torque is applied on the plasma. Modes rotating faster than the plasma provide a positive torque, resulting in radial compression. However, in 2018, we used the strong-drive regime to compress plasmas. This regime involves larger amplitude rotating electric field that do not couple the plasma to a specific mode. The electron and positron plasmas are thereby compressed from 5 mm to 0.5 mm in 300 s in the lower electrode stack. To compress antiproton plasmas, we use sympathetic compression where electrons and antiprotons are compressed at the same time in the strong-drive regime. With two species of particles, compressing one species with the rotating wall can cause the other species to follow via Coulomb collisions. The radii of both species get smaller as the compression time increases. Antiprotons rotate under the influence of the electron plasma's space charge because the number of antiprotons is small compared to the number of electrons. However, the antiproton cloud only compresses when slow electron plasma compression is used. We found that compression is more efficient when the rotating wall electrode is located at one end of a long plasma (Fig 4.3). After a certain amount of time, the plasma reaches a limited density and no more compression is possible.

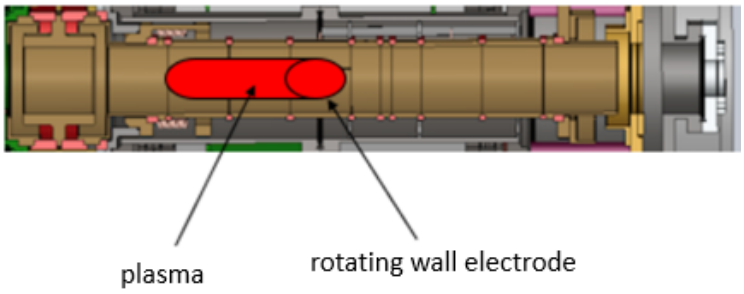

Figure 4.3: Compression of a plasma in the lower electrode stack.

To catch and cool positrons or antiprotons, the number of electrons used is very important. To get a fixed number of electrons and a fixed plasma radius at the same time, we use the strong-drive regime-evaporative cooling method [25]. Using this method, positron and electron plasmas are formed each trial in the same conditions to form trapped antihydrogen atoms. We combine the strong-drive regime of a rotating electric field and the evaporative cooling method (described more precisely later in this chapter).

In our procedure, the plasma is expanded from 1 electrode at 100 V to 3 electrodes at 100 V in 5 seconds in the lower electrode stack and the rotating electric field compresses the plasma (Fig 4.4.1). The well depth is reduced from one side of the plasma and some particles are sent onto the degrader electrode (Fig 4.4.2), at the bottom of the electrode stack. Finally, the rotating electric field compresses the plasma until it reaches the desired plasma radius (Fig 4.4.3). At the end, the plasma has a fixed radius and a fixed density.

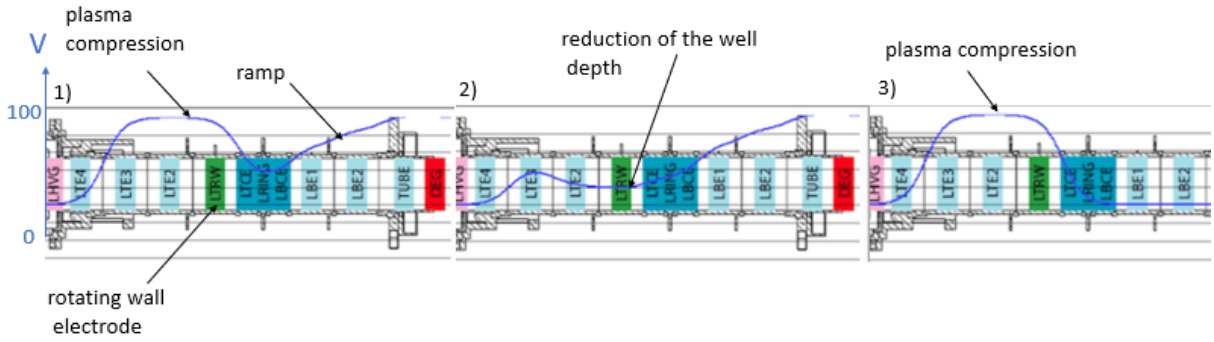

Figure 4.4: Strong-drive regime-evaporative cooling method.

4.1.3 Adiabatic transfer of particles

Once positron and antiproton plasmas are compressed to small radii, we move plasmas adiabatically from the lower electrode stack to the upper electrode stack (Fig 2.4). Antiprotons and positrons are moved next to each other in the upper electrode stack to form a nested well before the mixing sequence (Fig 4.5). However, moving particles can cause the plasma to expand or to increase its internal temperature. To counteract this effect, we move plasmas adiabatically with harmonic potentials.

A program generates electric potentials for the entire electrode stack and then calculate a table of potential derivatives to get a target curvature. We use the best target curvature to form harmonic potentials. The program is based on electrodes lengths and radii in the lower and upper electrode stack. The potential at any grid-point is found by setting $\nabla^2\phi = 0$. In cylindrical coordinates, with h the grid spacing, we have

$$\phi_{i,j} = \frac{1}{4}(\phi_{i-1,j} + \phi_{i+1,j} + \phi_{i,j-1} + \phi_{i,j+1} + \frac{h}{2\rho}(\phi_{i,j+1} - \phi_{i,j-1})). \tag{4.2}$$

Due to the $1/\rho$ term, the solution on-axis is

$$\phi_{i,0} = \frac{1}{6}(\phi_{i-1,0} + \phi_{i+1,0} + 4\phi_{i,1}). \tag{4.3}$$

Each grid point is 0.01 in away from the previous one. We apply 0 V at each endcap and to all of the electrodes except the one which is under consideration.

We use the relaxation method to generate grid of potentials. For each grid point, 4 grid points surround the grid point with the potential that is being relaxed. The output are electric potential values for each combination of z and r. We generate a table of functions defined around the center of each electrode. An on axis potential is generated for an electrode k at a position x. These functions are only defined for a few inches around the center of each electrode.

For each movement in the trap, we use at least 4 electrodes. We move the plasma back and forth between the lower electrode stack and the upper electrode stack and detect plasma modes to make sure the plasma is still in the same conditions.

4.1.4 Plasma cooling methods

We would like to cool plasmas to very low temperatures before the mixing sequence to form efficiently trapped antihydrogen atoms. Several techniques have been employed to cool particles (antiprotons cooling with embedded electrons [21] explained in the previous chapter, evaporative cooling [25] and adiabatic cooling [21]).

During adiabatic cooling, the depth of a confining potential is reduced (Fig 4.5). The plasma grows in length along the z axis but keeps the same radius. The plasma volume increases from a volume V_i to a volume V_f. The final plasma temperature is

$$T_f = (V_i/V_f)^{2/3} T_i, \tag{4.4}$$

where T_i is the initial plasma temperature (Fig 4.5). The adiabatic cooling method is also reversible. If we increase the depth of the confining potential, the plasma volume decreases and the plasma temperature increases. The adiabatic cooling method is used just before the mixing sequence (Fig 4.5).

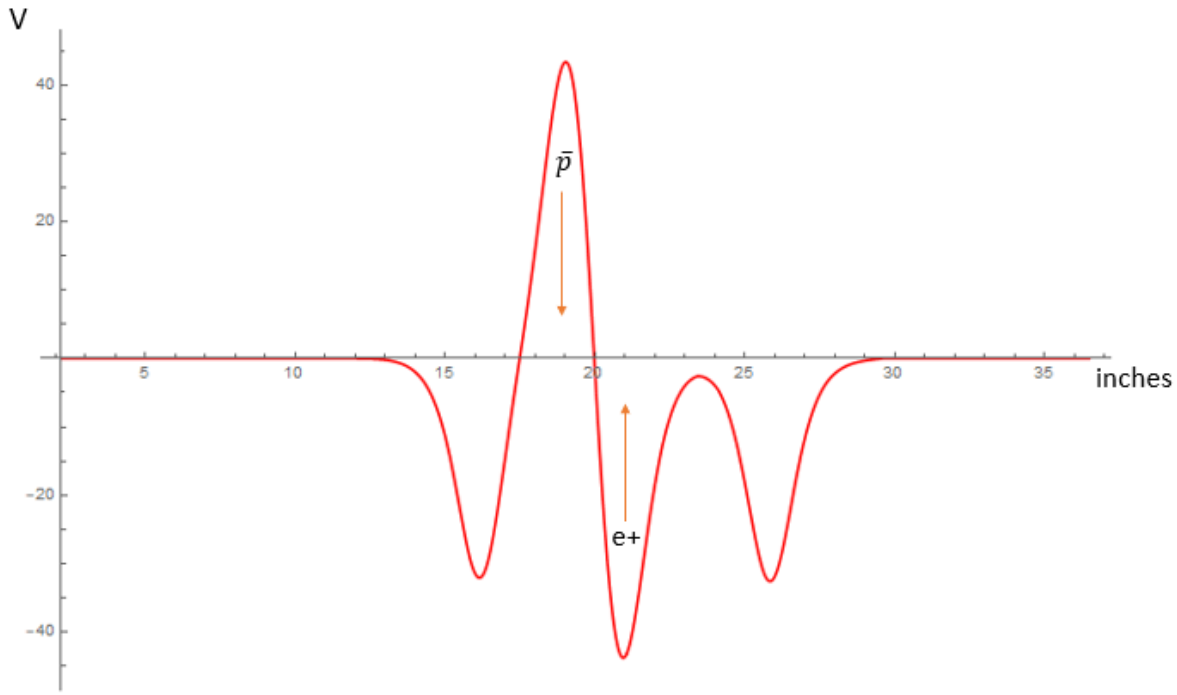

Figure 4.5: During the adiabatic cooling method, the depth of confining potentials are reduced. Plasmas grow in length along the z axis but keep the same radii.

We use an additionnal method to cool down even more the positron plasma before the mixing sequence (Fig 4.6.2). This is the evaporative cooling method, where the depth of the confining potential is reduced until hot positrons come out (Fig 4.6). After evaporative cooling, the remaining positrons in the trap re-thermalize to a lower temperature, but the plasma usually expands. This method allows to mix only the coldest positrons with antiprotons to form efficiently trapped antihydrogen atoms

(Fig 4.6.2).

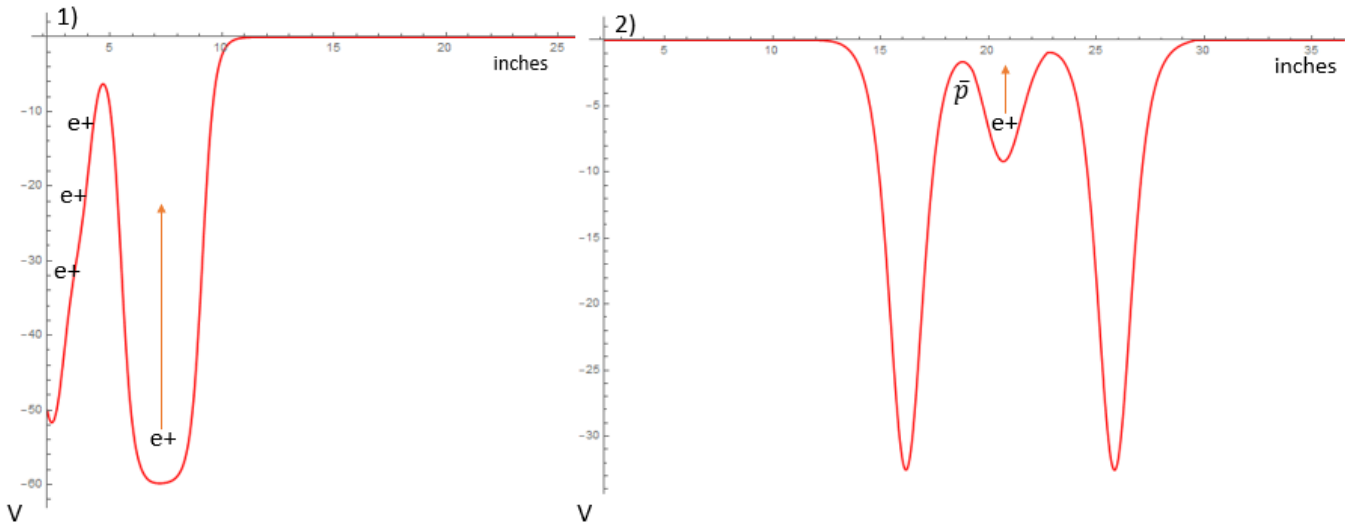

Figure 4.6: Evaporative cooling method: 1) Strong-drive regime-evaporative cooling method. The well depth is reduced from one side of the plasma. A negative voltage ramp is applied and positrons are attracted towards the bottom the trap; 2) Before the mixing sequence, the depth of the confining potential is reduced until hot positrons come out.

4.2 Antihydrogen trials and production of 5 trapped antihydrogen atoms per hour

In 2018, our ATRAP collaboration produced 5 trapped antihydrogen atoms per hour trial, in 9 demonstrative trials [24]. Plasmas manipulation techniques, described previously, were used for these trials.

4.2.1 Antihydrogen trial method

We report the method used in 2018, at the ATRAP experiment, to produce 5 trapped antihydrogen atoms per trial. At the beginning of a trial, a high random

number of electrons are caught into the lower electrode stack (1 min). A 4 mm electron plasma radius with 150 million electrons (1 min) is prepared with the strong-drive regime-evaporative cooling method (Fig 4.4). The electron plasma density is 1.5×10^8 cm^3. Then, positrons are loaded in the lower electrode stack for 14 min (Fig 3.2). The electron plasma is dumped out and the strong-drive regime-evaporative cooling method (Fig 4.6.1) forms a 0.5 mm positron plasma radius with 20 million particles (5 min). The positron plasma density is 5.1×10^8 cm^3. The positron plasma moves adiabatically in the upper electrode stack (1 min) and the field-boosting solenoid is ramped up to 14 Amp (3 min). A high random number of electrons are caught once again in the lower electrode stack using the excimer laser. A 6 mm electron plasma radius with 100 million electrons is prepared with the strong-drive regime-evaporative cooling method (1 min 30). The electron plasma density is 6.2×10^7 cm^3. We determined experimentally that if the ratio between the number of electrons and antiprotons is about 1000, the time that it takes to cool antiprotons is about 2 seconds in the 3.7 T field [20]. 360 000 antiprotons are loaded within 6 AD shots (12 min). A voltage of 1250 V is applied on the degrader electrode and a voltage of -5 kV is applied at the center of the electrode stack to make sure antiprotons do not access the upper electrode stack. Between each AD shot, the voltage on the degrader electrode is changed from 1250 V to -5 kV and antiprotons bounce through the electron plasma (Fig 4.7).

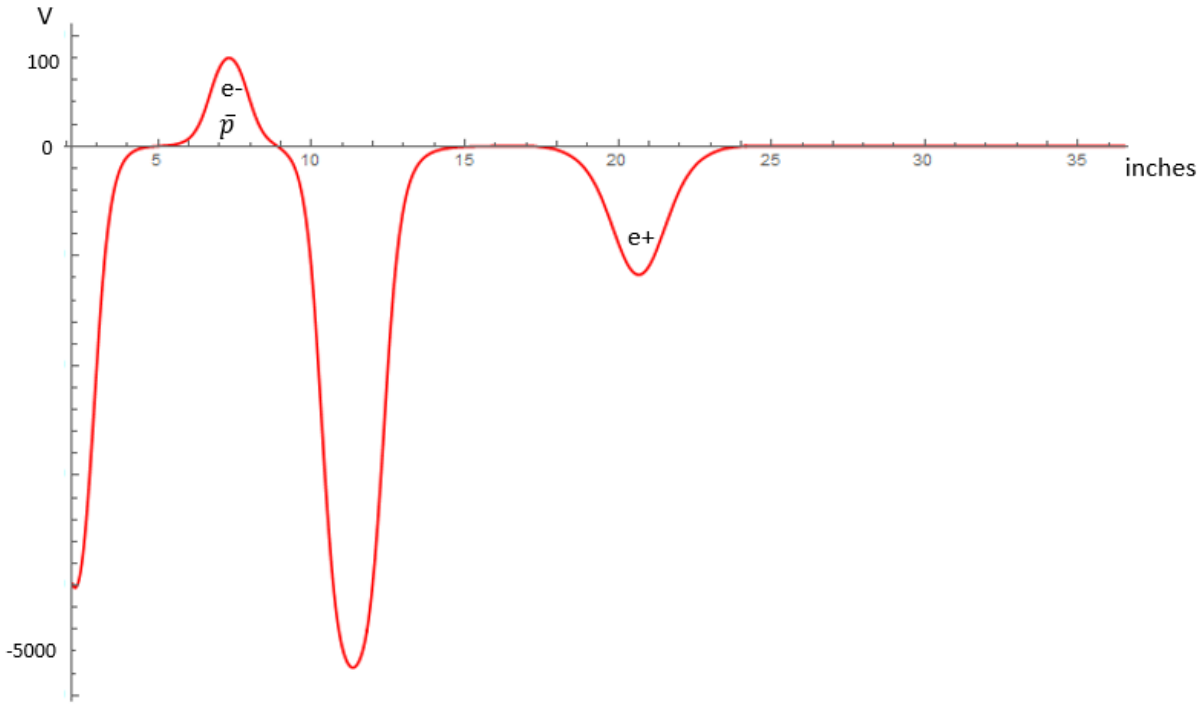

Figure 4.7: Antiprotons caught by the electron plasma. A negative high voltage of - 5 kV is applied on the DEG electrode at the bottom of the electrode stack and on the HV electrode located at the center of the electrode stack. Antiprotons bounce through the electron plasma. At the same time, positrons remain confined in the upper trap.

Some electrons are pulsed out from the antiproton cloud using a negative pulser to keep only 10 million electrons. Several short voltage pulses are applied for 100 ns. Antiprotons remain trapped since they are heavier and because they move much more slowly than electrons. Using sympathetic compression, the electron-antiproton plasma is compressed for 400 s. After compression, the electron-antiproton plasma radius is 1 mm. Most of the electrons are pulsed out from the antiproton cloud. Typically 900 electrons are kept to cool down the antiproton plasma. The antiproton plasma moves adiabatically from the lower electrode stack to the upper electrode stack. Once the antiproton plasma is in the upper electrode stack, the field-boosting

solenoid is ramped down (3 min). The nested well is formed and the Ioffe octupole trap is ramped up (4 min). The adiabatic cooling method reduces plasmas temperature (Fig 4.5) and the evaporative cooling method reduces the positron plasma temperature even more (Fig 4.6.2). The positron plasma radius is 1 mm and the antiproton plasma radius is 4 mm. The depth of the antiproton potential well is reduced in 10 s. Antiprotons bounce through the positron plasma due to the 2 negative potentials outside of the mixing well (Fig 4.8). Finally, the positron plasma potential well is reduced. Positrons may mix with some remaining antiprotons. Each trial takes about 1 hour.

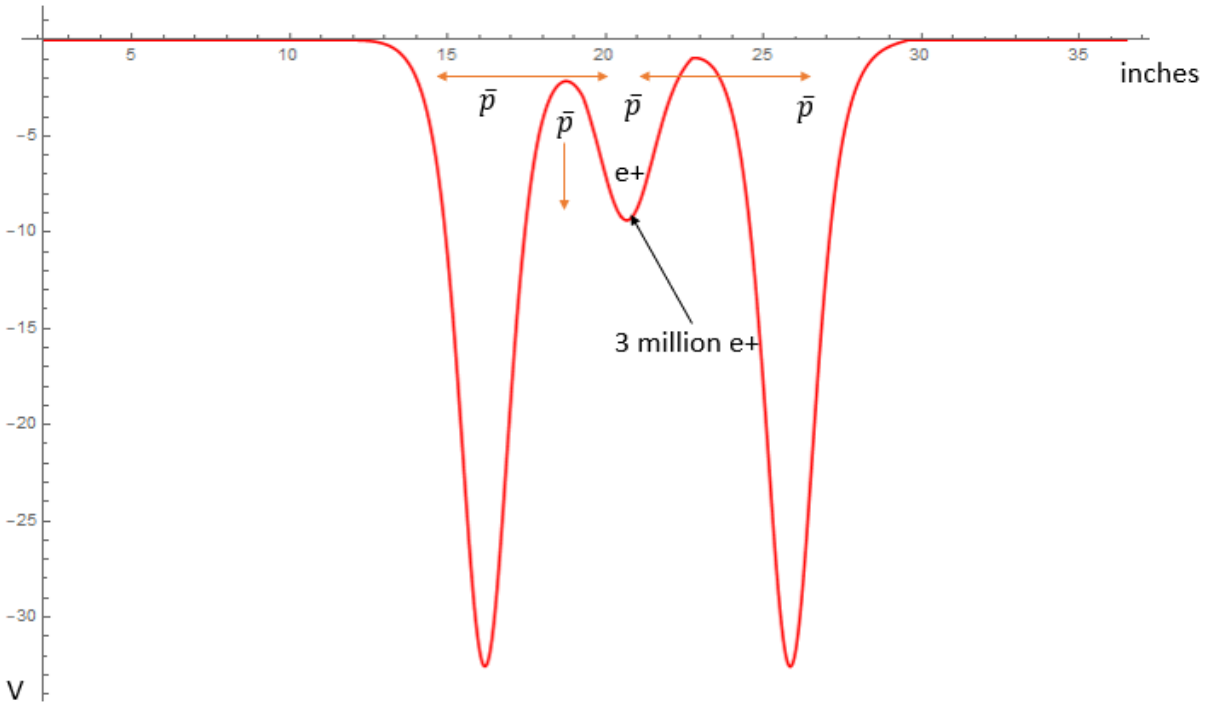

Figure 4.8: During the mixing sequence, the depth of the antiproton plasma potential well is reduced in 10 s. Antiprotons bounce through the positron plasma.

Other methods have been employed to mix plasmas in the past. In fact, $\bar{p}$ energies

can be excited using a rf drive or a noise drive, allowing them to climb the central barrier and interact with the e+. Antiprotons pass several times through the e+ cloud until they interact each other. Then, the depth of the e+ well is reduced. However, this method increases the antiproton plasma temperature.

4.2.2 Clearing electric field

To make sure no more charged particles remain mirror trapped, we sweep the trap with strong axial electric fields of ± 5 V/cm [43]. A 1 s delay is introduced between the end of the mixing sequence and the application of the clearing field to ensure that trapped antihydrogen atoms are sufficiently deeply bound so that they will not be ionized. These fields are large enough to eject any antiproton that could be trapped directly by the Ioffe pinch coils.

As an antiproton moves from a region of weak magnetic field to strong magnetic field, the cyclotron energy E_c increases to keep its magnetic moment $\mu_{\bar{p}} = E_c/|\vec{B}|$ invariant, and the translational kinetic energy E_T decreases to keep the total energy constant. If the antiproton moves into a field with $|\vec{B}|$ so large as to cause $E_T = 0$, the antiproton will reverse its trajectory and remains mirror trapped.

We would like to find the minimum translational kinetic energy E_T necessary to ensure that an antiproton, with an initial cyclotron energy E_c, will not be mirror-trapped. In the Ioffe octupole trap, B_{max}=1.6 T and B_0=1 T (Fig 2.7). As a consequence, an antiproton must have a kinetic energy $E_T \geq E_c(1.6 - 1) = 0.6E_c$ to avoid being mirror-trapped. When the potential ϕ is applied, an additional term $-q\phi$ must be added to the total energy. As a consequence, $E_T \geq E_c(\frac{B}{B_0} - 1) - q(\phi - \phi_0)$.

It is possible to satisfy the previous equation, for any E_c and B, if ϕ is made large enough. Here, B represents the magnetic field at the turning point, where the antiproton reverses his trajectory and remains "mirror trapped". In this case, we have $\phi \geq \frac{E_c}{2.66\times10^{-19}} + \phi_0$. An antiproton remains mirror-trapped if it stays in a local minimum of the pseudopotential throughout its entire trajectory. At E_c=137 eV [20], the pseudopotential has a local minimum. Antiprotons and positrons are cleared away by axial electric fields of $\phi \geq \pm$ 5.2 $V/cm + \phi_0$.

4.2.3 Results

When the Ioffe trap is quickly de-energized, trapped antihydrogen atoms escape and create detectable annihilation signals due to high energy pions. All particles are dumped within 50 ms (Fig 4.9). We use detectors such as scintillating fibers and paddles to detect antihydrogen atoms. In 2018, our trigger to detect one antihydrogen atom was a coincidence between 2 fibers (fiber trigger). We were monitoring a 150 ms time window that starts with the trigger to dump the octupole trap. On average, for a total of 9 trials [24], we detected 5.2 antihydrogen atoms per trial (Fig 4.9).

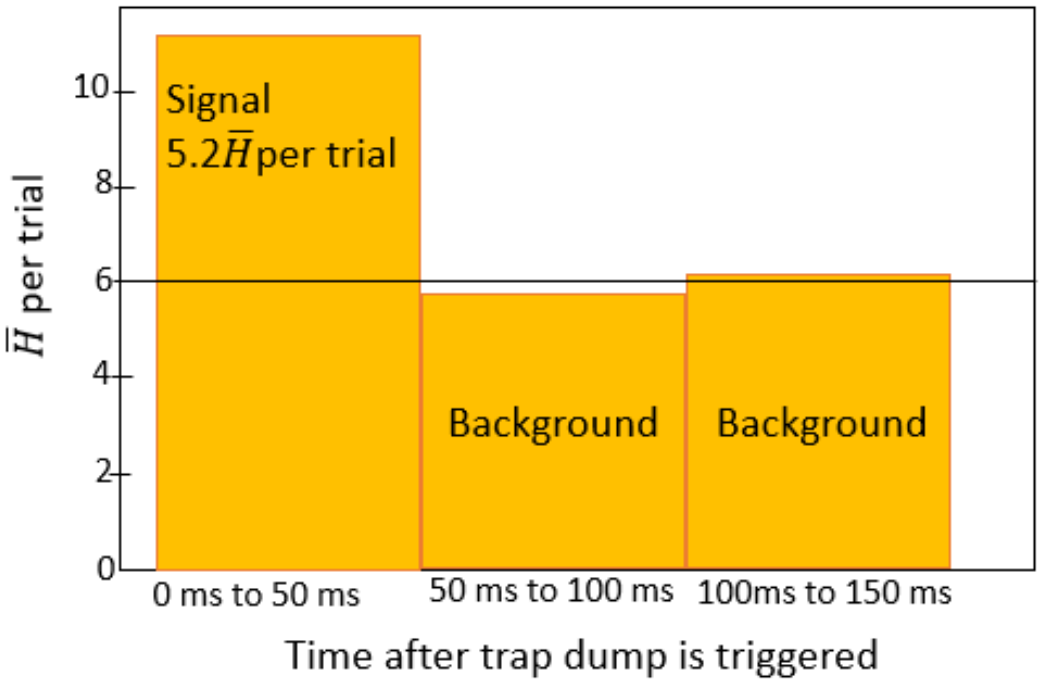

Figure 4.9: Antihydrogen detection.

The efficiency of the fiber singles for seeing a $\bar{p}$ annihilation within the trap is 80 % as explained in chapter 2. By spilling trapped antiprotons to calibrate detectors, we determined the relative efficiency between fiber singles (F1) and fiber trigger (FT), F1=3FT. As a consequence, the conversion from trigger counts to $\bar{p}$ annihilations is 3 counts/0.8 = 3.75 $\bar{p}$. There is approximately one antihydrogen count for every 3.75 $\bar{p}$ annihilations. In the next table, we represent intervals from 0 to 50 ms (a), from 50 ms to 100 ms (b), and from 100 ms to 150 ms (c).

MCS datas					
N trial	FTa	FTb	FTc	FTsignal	FTbackground
1	2	3	2	-0.5	2.5
2	4	0	3	2.5	1.5
3	5	2	2	3	2
4	2	0	0	2	0
5	3	2	4	0	3
6	6	0	0	6	0
7	3	3	0	1.5	1.5
8	0	3	1	-2	2
9	2	1	3	0	2
Sum	27	14	15	12.5	14.5
Ave	3	1.5556	1.6667	1.38889	1.61111

To extract the number of trapped antihydrogen atoms, we determine the difference between the number of counts within 50 ms and background counts, FT1signal=FTa-FTbackground=12.5. As a consequence $12.5 \times 3.75 \approx 46.9$ $\bar{H}$. In 9 trials, 46.9 trapped antihydrogen atoms were detected. This represents 5.2 trapped antihydrogen atoms per trial (Fig 4.9). The standard deviation of the poisson distribution for fiber trigger counts is (12.5±5.8) events. The standard deviation of the poisson distribution for background counts is (14.5±2.7) events.

As a conclusion, we succesfully formed 5 trapped antihydrogen atoms per hour

long trial [24]. Plasmas manipulations techniques were used to form reproducible plasmas during each trial. In the next chapter, a new design of the electrode stack is proposed to produce much more trapped antihydrogen atoms and measure precisely the 1S-2S transition.

Chapter 5

Proposed design of the apparatus

5.1 Introduction

To measure more precisely the 1S-2S transition, we would like to produce more trapped antihydrogen atoms per trial and accumulate $\bar{H}$ atoms in the Ioffe octupole trap. If 10 trapped antihydrogen atoms are formed every 4 min, 150 $\bar{H}$ atoms could be confined in 1 hour in the Ioffe octupole trap, using the accumulation method. However, we would need to prepare positron and antiproton plasmas at the correct temperature, density and geometry in the Penning-Ioffe trap and simultaneously confine trapped antihydrogen atoms.

For this purpose, a new design of the electrode stack is proposed in this chapter (Fig 5.1B). The proposed electrode stack has more electrodes than the one used in 2018 (Fig 5.1A). We could prepare efficiently plasmas on the two sides of the trap and mix at the same time positrons and antiprotons at the Ioffe trap minimum (Fig 5.3).

At the ATRAP experiment, each trial was performed in 1 hour in 2018. With more electrodes and new rotating wall electrodes (Fig 5.1B), we will see that we could form trapped antihydrogen atoms much faster than before.

5.2 Proposed electrode stack and antihydrogen trial

In 2018, the electrode stack had 32 electrodes with 2 rotating wall electrodes (Fig 5.1A). The proposed electrode stack has 41 electrodes with 4 rotating wall electrodes (Fig 5.1B). There is a new upper electrode stack with 6 electrodes to load and prepare positrons away from the Ioffe trap field (Fig 5.1B). A new rotating wall electrode (Fig 5.1B - RW 1) will compress positrons in the upper trap. In the middle trap, two new rotating wall electrodes (Fig 5.1B - RW 2 and RW 3) will compress positron and antiproton-electron plasmas before the mixing sequence (Fig 5.1B).

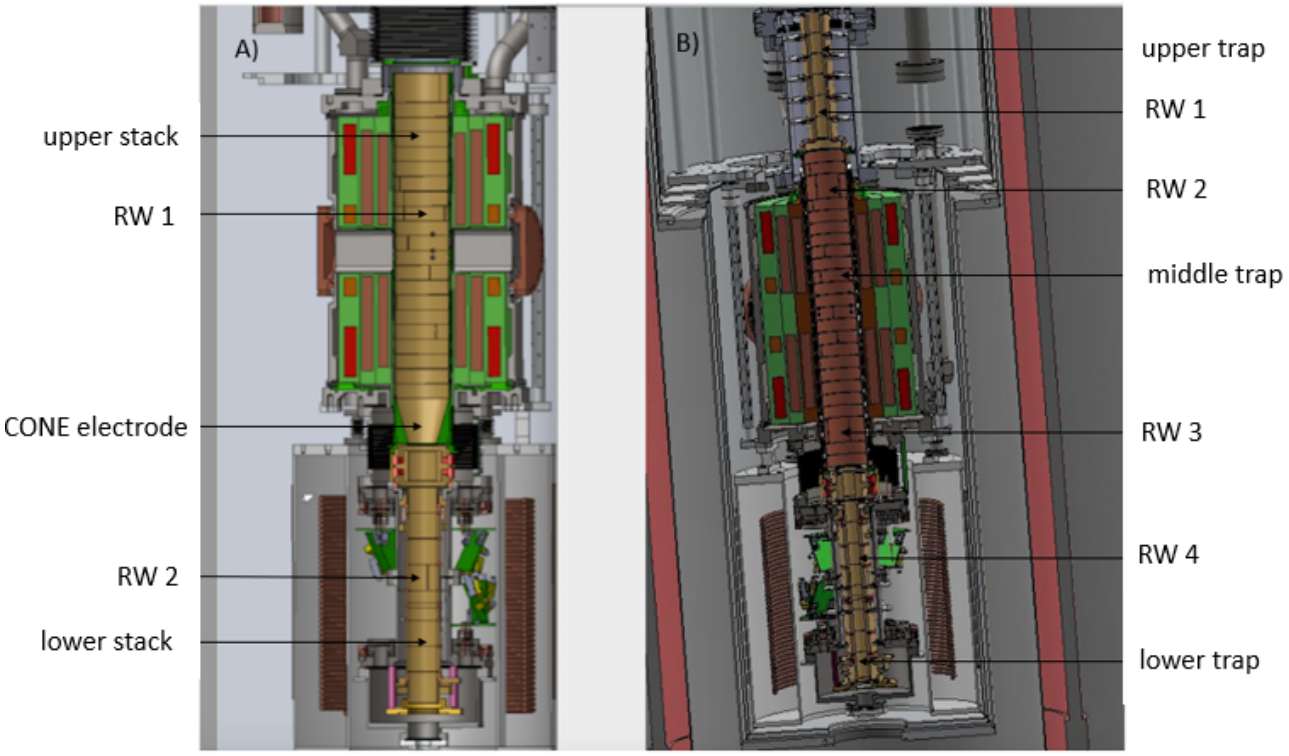

Figure 5.1: Comparison of the electrode stack used in 2018 (A) and the proposed electrode stack (B).

We could produce quickly and accumulate trapped antihydrogen atoms in the Ioffe octupole trap with a new method. With the strong-drive regime-evaporative cooling method [25], two electrons plasmas could be prepared at the same time in the upper trap and in the lower trap. Once the 2 electron plasmas have the correct density and geometry, positrons and antiprotons are loaded simultaneously. Then, the electron-antiproton plasma and the positron plasma are compressed to small radii on the two sides of the trap (Fig 5.2).

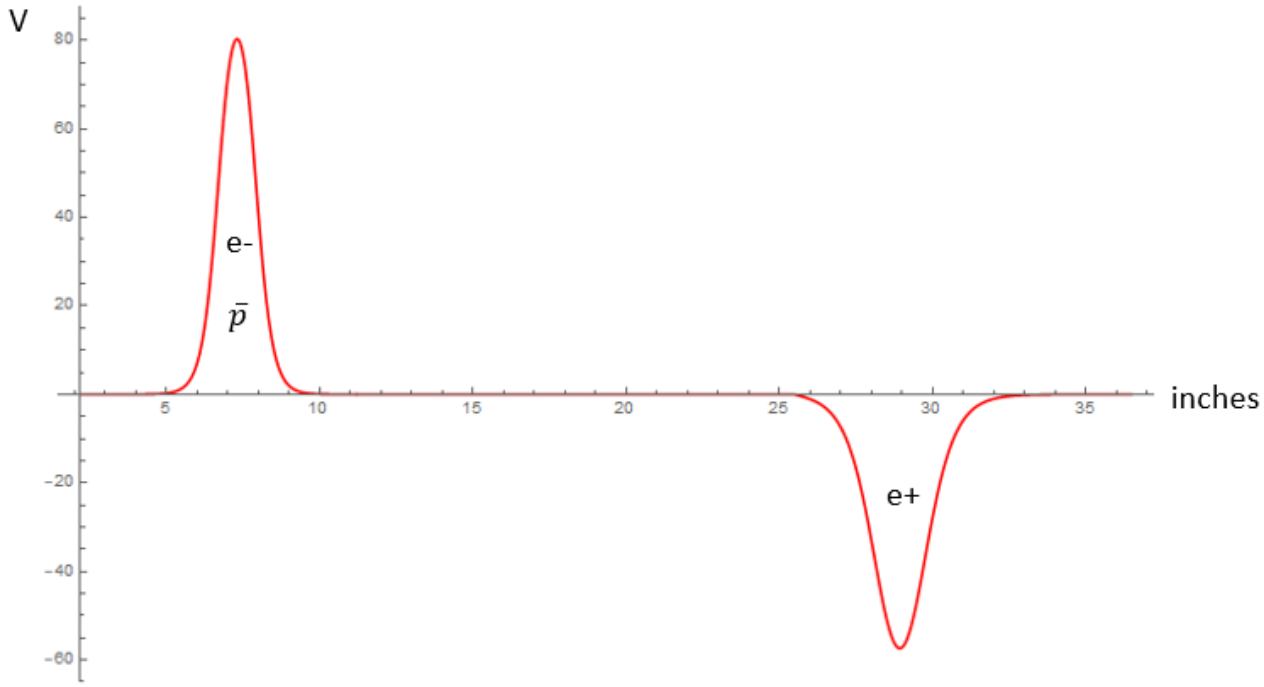

Figure 5.2: Antiproton and positron plasmas are prepared simultaneously.

The strong-drive regime-evaporative cooling method [25] forms a compressed positron plasma with a fix number of particles. Some electrons are pulsed out from the electron-antiproton cloud. The electron-antiproton plasma and the positron plasma move adiabatically in the middle trap simultaneously. Plasmas are compressed again in the middle trap and most of electrons are pulsed out from the electron-antiproton cloud. The strong-drive regime-evaporative cooling method prepares two new electrons plasmas in the lower trap and in the upper trap for the next trial. At the same time, the positron and the antiproton plasma move near the Ioffe trap minimum in the middle trap (fig 5.3). The antiproton and positron plasmas mix to form trapped antihydrogen atoms. Electron plasmas in the upper trap and in the lower trap with the correct geometry and density catch again positrons and antiprotons.

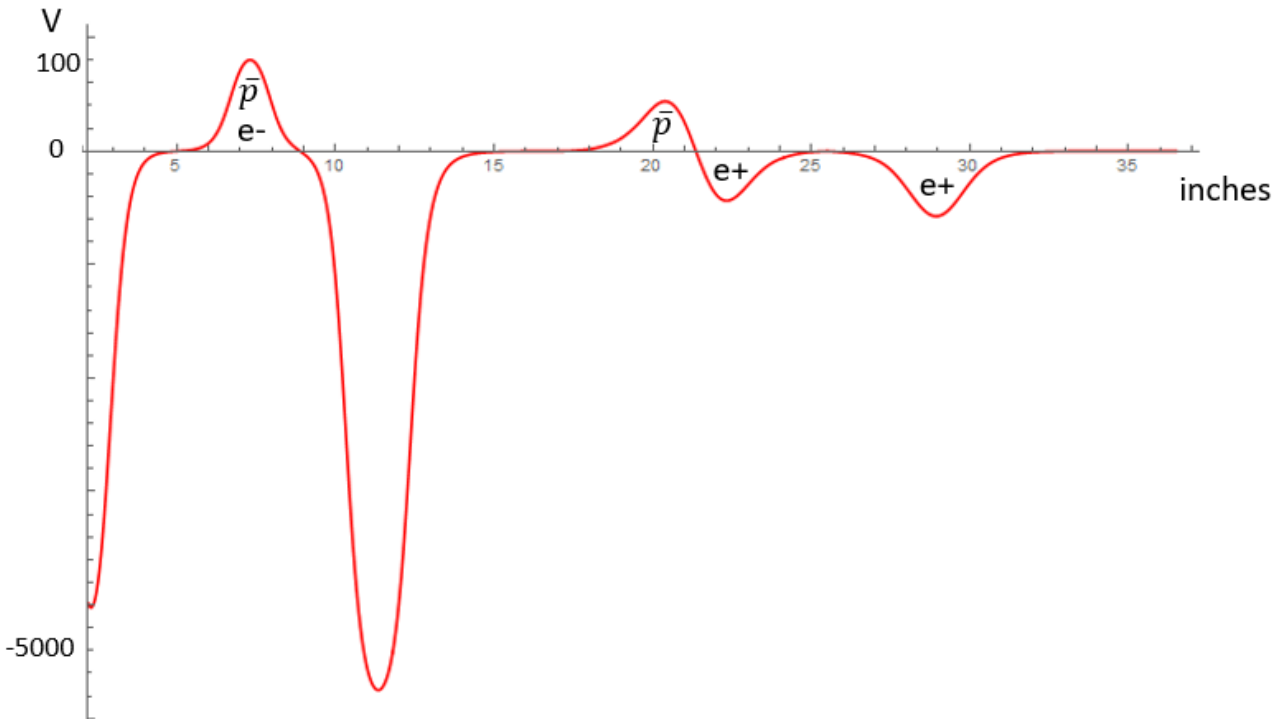

Figure 5.3: Mixing sequence and preparation of a new antihydrogen trial.

With this new method, each trial could be done much faster than before. At the end of multiple trials, many trapped antihydrogen atoms could be confined in the Ioffe octupole trap. We could measure more precisely the 1S-2S transition of antihydrogen atoms.

5.3 XY translation stage replacement

To provide the volume needed to add more electrodes in the apparatus, we replaced the XY translation stage (Fig 2.9). The XY translation stage used in 2018 moves very slowly at cryogenic temperatures and takes a huge amount of space in the apparatus due to the long bellows (Fig 2.9). These long bellows move with the stage in the X

and Y direction under vacuum.

In 2019, a rotatable stage (Fig 5.4) has been designed to replace the XY translation stage (Fig 2.9). By turning a flexible shaft (Fig 5.4), a stage rotates to either image plasmas or align and send the excimer laser in the experiment space through a 1.5 mm diameter hole (Fig 5.4A). This 1.5 mm diameter hole is surrounded by faraday cups. The lyman-alpha laser and positrons can access the trap via a 6 mm diameter hole. The 6 mm diameter hole is also surrounded by faraday cups (Fig 5.4A).

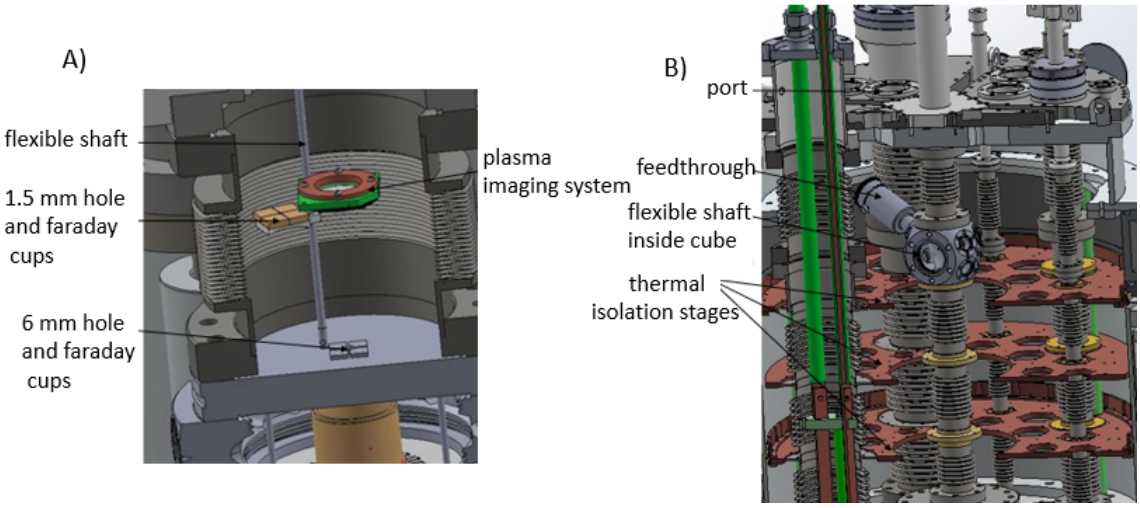

Figure 5.4: New rotatable stage.

The flexible shaft is connected to a cryogenic rotatable feedthrough inside a cube in the upper thermal isolation stage, where the temperature is about 75 K (Fig 5.4B). This cryogenic rotatable feedthrough turns the flexible shaft. A motor at room temperature is connected to the feedthrough via a port above the apparatus (Fig 5.4B). This port was used initially for the XY stage motors. To move the rotatable stage, long edge-welded bellows are not required and multiple new electrodes can be added in the electrode stack instead (Fig 5.1).

However, the flexible shaft induces heat load in the apparatus due to its temperature gradient from 4 K to 75 K. For this reason, we would like to determine how much energy does the shaft dissipates into the apparatus. The heat conduction is defined as [44]

$$Q = \frac{A}{L}\int_{T1}^{T2} \lambda(T)dT \tag{5.1}$$

with A the cross section, L the length of the shaft and $\lambda(T)$ the temperature-dependent thermal conductivity. For a shaft of 1 m, with a thickness of 0.5 mm, an outer radius of 5.8 mm, Q_f=5.4 mW.

Using stainless steel, we would boil off less than 0.12 mL of liquid helium per hour due to the flexible shaft. This is very small in comparison to the 11 L/h of liquid helium that boils off due to the experiment. If the heat load is determined between the 4 K and the 20 K region, the boil off rate due to the shaft would be 0.02 mL/h. Between the 20 K and the 75 K region, the boil off rate would be 0.1 mL/h. As a consequence, the heat load would not have a bad impact on the experiment.

5.4 Electrode stack modifications

5.4.1 Electrodes

In the proposed electrode stack, electrodes in the upper trap have the same dimensions as electrodes in the lower trap (Fig 5.1). They are made of gold-plated copper and have a 18 mm inner radius. These electrodes are separated by macor spacers. However, electrodes in the middle trap have a 33 mm innner radius and are separated by peek sleeves to better avoid shorts between electrodes (Fig 5.5B). In the

past, copper rings were epoxied within a G10 support sleeve (Fig 5.5A).

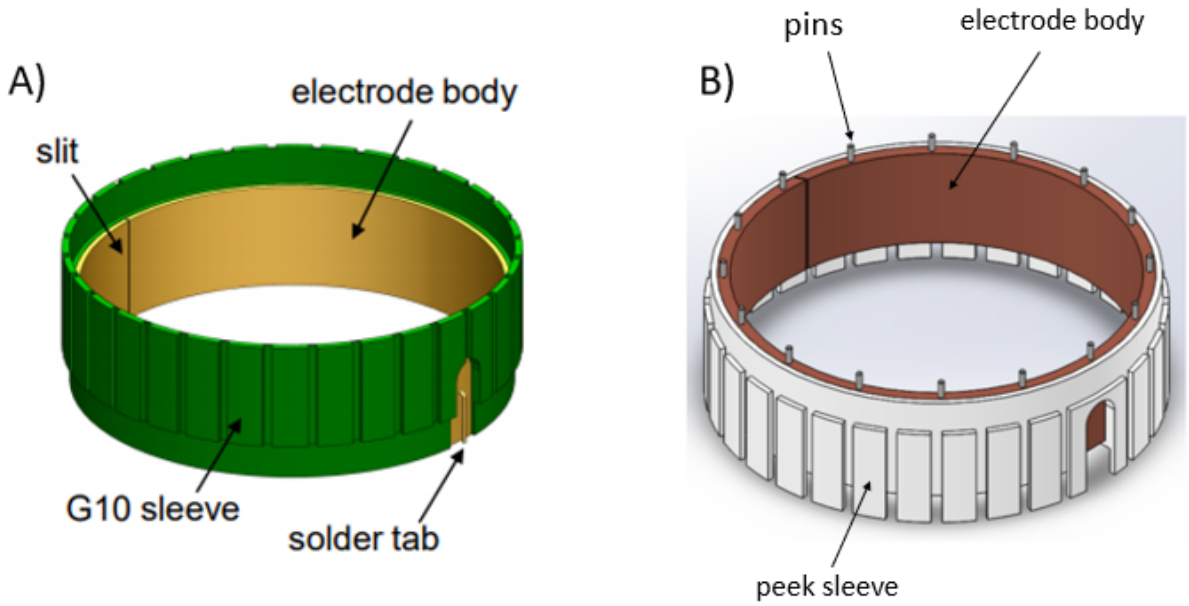

Figure 5.5: Comparison of electrodes used in 2018 in the upper stack (A) and new electrodes in the middle trap (B).

In addition to add electrodes in the electrode stack, we also replaced the CONE electrode (Fig 5.1A). The CONE electrode was located at the junction between the lower electrode stack and the upper electrode stack (Fig 2.4). However, small plasmas radii are not affected when moving adiabatically from a small electrode diameter (35 mm) to a big electrode diameter (68 mm). As a consequence, we replaced the CONE electrode (53 mm length) by several electrodes at fix radii (17.5 mm length, 68 mm diameter) to manipulate plasmas with more electrodes in the middle trap.

5.4.2 Rotating wall electrodes

In 2018, to compress a plasma from 5 mm to 0.5 mm at 3 Vpp in the lower electrode stack (Fig 5.1A), the rotating electric field was applied for at least 300 s.

In the upper electrode stack (Fig 5.1A), electrodes radii are twice bigger in diameter (68 mm diameter 17.3 mm length). It is even more difficult to compress plasmas in a short amount of time.

To accumulate trapped antihydrogen atoms effectively, we would need to compress plasmas to small radii much faster. To compare the electric field applied at the center of a plasma, for different electrodes dimensions (Fig 5.6), we solve the laplace equation in cylindrical coordinates $\nabla^2\Phi = 0$. We consider that the top and bottom of the cylinder are grounded far away from the single rotating wall electrode under consideration. In the following equation, (h) represents the heigh of the rotating wall electrode and (a) the radius of the rotating wall electrode,

$$\Phi(\rho,\phi,z) = \sum_{m=0}^{inf}\sum_{n=1}^{inf} A_{mn}\cos(m\phi)\cos(n\pi z/h)I_m(n\pi\rho/h) \tag{5.2}$$

With

$$A_{mn} = (2-\delta_{m0})\frac{(\int_{-h/2}^{h/2} dz\cos(n\pi z/h)V(z))(\int_0^{2\pi} d\phi\cos(m\phi)V(\phi))}{2\pi h I_m(n\pi a/h)} \tag{5.3}$$

The number of quadrants in the rotating wall electrode is taken into account in the potential V_ϕ. The electric field applied at the center of the trap as a function of radius to height ratio is

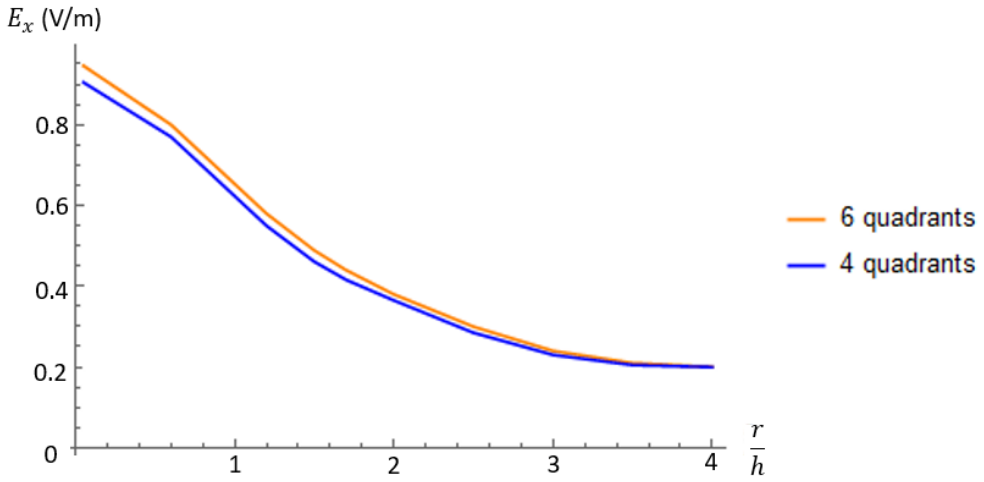

Figure 5.6: Electric field applied at the center of the trap versus radius to height ratio.

For a given rotating wall strength, the required voltage depends on the symmetry of the rotating wall, the number of split electrodes, the length and the radius of the rotating wall electrode. As the radius of the rotating wall electrode increases, the voltage that must be applied to that electrode in order to maintain a given rotating wall strength, will increase (Fig 5.6). As the length of the electrode increases, the required voltage will decrease (Fig 5.6).

For a given voltage and based on electrodes dimensions, the lower stack rotating wall (35 mm diameter, 30.7 mm length) used in 2018 applies a rotating electric field 4 times stronger at the center of a plasma than the upper stack (68 mm diameter, 17.3 mm length) rotating wall (Fig 5.1A). This is the reason why, we need more time to compress a plasma with the upper stack rotating wall. In the proposed electrode stack, if the length of rotating wall electrodes is increased from 17.3 mm to 35.5 mm in the middle trap (Fig 5.1B) and if the number of quadrants is increased from 4 to 6, the electric field, applied at the center of a plasma, would be 1.8 times stronger than

before, for a given voltage (Fig 5.1B). As a consequence, we could compress plasmas to small radii faster.

In addition, employing 6 quadrants instead of 4 gives a better rotating wall in that undesirable Fourier components. The purity of the rotating potential is improved. The drive usually results in some plasma heating, and additional heating can arise with unwanted spatial harmonics due to the finite size of sectored electrodes. Finally, using these new rotating wall electrodes in the middle trap, antiproton and positron plasmas could be prepared at 1 mm radius before the mixing sequence, which is essential for the antihydrogen production. With the new electrode stack design, we could produce, as a consequence, much more trapped antihydrogen atoms per trial, in a short amount of time, and accumulate antihydrogen atoms in the Ioffe octupole trap.

Chapter 6

Conclusion

Magnetic field stability, laser stability, a good detector system and enough trapped atoms are required to measure precisely the 1S-2S transition of antihydrogen atoms. The Lyman-alpha laser could reduce velocity-dependent systematic shifts by slowing down and cooling down antihydrogen atoms. By driving out $1S_c$ states with microwaves, we could measure the $1S_d$-$2S_d$ transition, using the 243 nm laser. Finally, to achieve a good comparison between the 1S-2S transition of antihydrogen and hydrogen atoms and verify CPT symmetry at a higher level of precision, we have to compare the 1S-2S transition in the same environment. This could reduce the Zeeman shift and the DC Stark shift.

At the ATRAP experiment, a new octupole trap with a faster magnet dump was used to confine and detect trapped antihydrogen atoms [24]. Within our Penning trap, positrons and antiprotons were confined simultaneously to produce efficiently trapped antihydrogen atoms. Only plasmas at a certain density, geometry and temperature form $\bar{H}$ atoms in the Ioffe trap. Most of antihydrogen atoms are formed by three-body

recombination which requires a high positron density and low plasmas temperature. Using our rotating wall electrode in the lower electrode stack, we were able to compress in 2018 the electron-antiproton plasma and the positron plasmas to small radii (1 mm). Then, using the adiabatic cooling method and the evaporative cooling method, positrons and antiprotons were cooled as much as possible before the mixing sequence.

To make efficiently trapped antihydrogen atoms and determine plasma characteristics, diagnostics were improved at the ATRAP experiment. A new plasma imaging system has been implemented on the XY translation stage [24]. In 2018, for the first time, we were able to characterize positron and antiproton plasmas before the mixing sequence. However, this diagnostic requires to send particles onto a phosphor screen. Consequently, we improved the plasma modes system to quickly characterize plasmas in the Penning trap without loosing particles. The sensitivity of the plasma modes system has been improved by a factor of 10. We were able to detect plasma modes with only 2 million particles in the lower electrode stack.

By improving diagnostics, we also improved plasma manipulation techniques. The strong-drive regime-evaporative cooling method [25] was developed in 2018. This method fixes electron and positron plasmas densities and forms reproducible plasmas during each antihydrogen trial. As a consequence, we produced 5 trapped antihydrogen atoms per hour long trial [24]. With a faster magnet dump, the cosmic ray signals that could be confused with annihilations from $\bar{H}$, were reduced.

To produce even more trapped antihydrogen atoms, a new electrode stack design has been proposed in 2019. The new electrode stack has more electrodes to prepare positron and antiproton plasmas simultaneously and confine at the same time trapped

antihydrogen atoms in the Ioffe trap. Antiproton and positron plasmas could be prepared quickly at 1 mm radius before the mixing sequence. To provide the volume needed to add more electrodes in the apparatus, we replaced the XY translation stage with a rotatable stage.

In the future, with the ELENA upgrade at CERN, we could load 100 times more antiprotons at lower energy per AD shot to produce even more antihydrogen atoms. The measurement of the 1S-2S transition of antihydrogen atoms will certainly improve with the demonstration of laser-cooling.

Bibliography

[1] Dolgov and Zeldovich. Rev. Mod. Phys. **53**, 1 (1981).

[2] O. Bertolami, Don Colladay, V. Alan Kostelecký, R. Potting. *CPT Violation and Baryogenesis*. Phys. Lett. B **395**, 178 (1997).

[3] C. S. Wu, E. Ambler, R. W. Hayward, D. D. Hoppes, and R. P. Hudson. *Experimental Test of Parity Conservation in Beta Decay.* Phys. Rev. **105**, 1413 (1957).

[4] J. H. Christenson, J. W. Cronin, V. L. Fitch, and R. Turlay. *Evidence for the 2π Decay of the K02 Meson.* Phys. Rev. Lett. **13**, 138 (1964).

[5] Christian G. Parthey et al. *Improved Measurement of the Hydrogen 1S - 2S Transition Frequency.* Phys. Rev. Lett. **107**, 203001 (2011).

[6] Particle Data Group (M. Tanabashi et al.) *Review of Particle Physics.* Phys.Rev. D **98** (2018) no.3, 030001 (2018).

[7] R. S. Van Dyck, Jr., P. B. Schwinberg, and H. G. Dehmelt. Phys. Rev. Lett. **59**, 26 (1987).

[8] G. Gabrielse, A. Khabbaz, D. S. Hall, C. Heimann, H. Kalinowsky, and W. Jhe.

Precision Mass Spectroscopy of the Antiproton and Proton Using Simultaneously Trapped Particles. Phys. Rev. Lett. **82**, 3198 (1999).

[9] M. Ahmadi et al. *Characterization of the 1S–2S transition in antihydrogen.* Nature, **557**, 71 (2018).

[10] O. Chamberlain, E. Segrè, C. Wiegand, and T. Ypsilantis, Phys. Rev. **100**, 947 (1955).

[11] G. Gabrielse, X. Fei, K. Helmerson, S. L. Rolston, R. L. Tjoelker, T. A. Trainor, H. Kalinowsky, J. Haas, and W. Kells, Phys. Rev. Lett. **57**, 2504 (1986).

[12] G. Gabrielse, S. L. Rolston, L. Haarsma, and W. Kells. *Possible antihydrogen production using trapped plasmas.* Hyperfine Interactions, **44**, pages287–293 (1989).

[13] G. Gabrielse, N. S. Bowden, P. Oxley, A. Speck, C. H. Storry, J. N. Tan, M. Wessels, D. Grzonka, W. Oelert, G. Schepers, T. Sefzick, J. Walz, H. Pittner, T. W. Hänsch, and E. A. Hessels, Phys. Rev. Lett. **89**, 233401 (2002).

[14] M. Amoretti et al. (ATHENA Collaboration), Nature **419**, 456 (2002).

[15] C. H. Storry et al. Phys. Rev. Lett. **93**, 263401 (2004).

[16] G. Gabrielse, P. Larochelle, D. Le Sage, B. Levitt, W. S. Kolthammer, R. McConnell, P. Richerme, J. Wrubel, A. Speck, M. C. George, D. Grzonka, W. Oelert, T. Sefzick, Z. Zhang, A. Carew, D. Comeau, E. A. Hessels, C. H. Storry, M. Weel, and J. Walz. *Antihydrogen Production within a Penning-Ioffe Trap.* Phys. Rev. Lett. **100**, 113001 (2008).

[17] G. Gabrielse, P. Larochelle, D. Le Sage, B. Levitt, W. S. Kolthammer, R. McConnell, P. Richerme, J. Wrubel, A. Speck, M. C. George, D. Grzonka, W. Oelert, T. Sefzick, Z. Zhang, A. Carew, D. Comeau, E. A. Hessels, C. H. Storry, M. Weel, and J. Walz, Phys. Rev. Lett. **100**, 113001 (2008).

[18] G. B. Andresen et al. *Confinement of antihydrogen for 1,000 seconds.* (ALPHA Collaboration), Nature Physics **7**, 558 (2011).

[19] G. Gabrielse, R. Kalra, W. S. Kolthammer, R. McConnell, P. Richerme, et al. *Trapped Antihydrogen in Its Ground State.* Phys. Rev. Lett. **108**, 113002 (2012).

[20] Philip John Richerme. *Thesis, Trapped Antihydrogen in its Ground State.* Harvard University, May 7, 2012.

[21] G. Gabrielse et al. *Adiabatic Cooling of Antiprotons.* Phys. Rev. Lett. **106**, 073002 (2011).

[22] M. Ahmadi et al. *Antihydrogen Accumulation For Fundamental Symmetry Tests.* Nature Comm. **8**, 681 (2017).

[23] Rita Kalra. *Thesis, An Improved Antihydrogen Trap.* Harvard University, 2014.

[24] E. Tardiff, X. Fan, G. Gabrielse, D. Grzonka, C. Hamley, E. A. Hessels, N. Jones, G. Khatri, S. Kolthammer, D. Martinez Zambrano, C. Meisenhelder, T. Morrison, E. Nottet, E. Novitski and C. H. Storry. *Two-Symmetry Penning-Ioffe Trap for Antihydrogen Cooling and Spectroscopy,* arXiv:2003.05032 (2020).

[25] M. Ahmadi et al. (ALPHA Collaboration). *Enhanced Control and Reproducibility of Non-Neutral Plasmas.* Phys. Rev. Lett. **120**, 025001 (2018).

[26] L.S. Brown and G.Gabrielse. *Geonium Theory: Single Electrons and Ions in a Penning Trap.* Rev. Mod. Phy. **58**,233-311 (1986).

[27] G.Gabrielse, L.Haarsma and S.L Rolston. *Open-Endcap Penning traps for high precision Experiments.* International Journal of Mass Spectrometry and Ion Processes, Volume **88**, Issues 2–3, 1 April 1989, Pages 319-332, https://doi.org/10.1016/0168-1176(89)85027-X.

[28] G. Bendiscioli and D. Kharzeev, La Rivista Del Nuovo Cimento Series 3 17, 1 (1994).

[29] I. D. Setija et al. *Optical cooling of atomic hydrogen in a magnetic trap.* Phys.Rev. Lett. **70**, 2257 (1993).

[30] G. Gabrielse, B. Glowacz, D. Grzonka, C. D. Hamley, E. A. Hessels, N. Jones, G. Khatri, S. A. Lee, C. Meisenhelder, T. Morrison, E. Nottet, C. Rasor, S. Ronald, T. Skinner, C. H. Storry, E. Tardiff, D. Yost, D. Martinez Zambrano, and M. Zielinski. *Lyman alpha source for laser cooling antihydrogen (2018). Opt. Lett.* **43**, 2905-2908 (2018).

[31] B. Levitt, G. Gabrielse, P. Larochelle, D. Le Sage, W.S. Kolthammer, R. McConnell, J. Wrubel, A. Speck, D. Grzonka, W. Oelert, T. Sefzick, Z. Zhang, D. Comeau, M.C. George, E.A. Hessels, C.H. Storry, M. Weel, and J. Walz, *Single-Component Plasma of Photoelectrons.* Phys. Lett. B **656**, 25-29 (2007).

[32] M. Hori et al. *Physics at CERN's Antiproton Decelerator.* Volume **72**, Pages 206-253, (2013).

[33] G.Gabrielse, S.L.Rolston, L.Haarsma, W.Kells. *Antihydrogen Production Using Trapped Plasmas.* Physics Letters A, Volume **129**, Issue 1, Pages 38-42, (1988).

[34] Michael E. Glinsky and Thomas M. O Neil. *Guiding center atoms: TBR in a strongly magnetized plasma.* Physics of Fluids B Plasma Physics **3**,5 (1991).

[35] G. Gabrielse et al. *Laser-Controlled Antihydrogen Production by Two-Stage Charge Exchange.* AIP Conference Proceedings 796, (2005).

[36] E. A. Hessels, D. M. Homan, and M. J. Cavagnero, Phys. Rev. A **57**, 1668 (1998).

[37] M. Charlton, S. Jonsell, L.V. Jorgensen, N. Madsen and D.P. van der Werf. *Antihydrogen for precision tests in physics.* Vol. **49**, (2008).

[38] M. D. Tinkle, R. G. Greaves, C. M. Surko, R. L. Spencer, and G. W. Mason. Phys. Rev. Lett. **72**, 352 (1994).

[39] G.Gabrielse, L.Haarsma and S.L Rolston. *Open-Endcap Penning traps for high precision Experiments.* International Journal of Mass Spectrometry and Ion Processes, Volume **88**, Pages 319-332, (1989), https://doi.org/10.1016/0168-1176(89)85027-X.

[40] D. H. E. Dubin. Phys. Rev. Lett. **66**, 2076 (1991).

[41] D. H. E Dubin. Phys. of Fluids B **5**, 295 (1993).

[42] François Anderegg. *Rotating Wall Technique.* CERN https://indico.cern.ch.

[43] P. Richerme,1 G. Gabrielse, S. Ettenauer, R. Kalra, E. Tardiff, D. W. Fitzakerley, M. C. George, E. A. Hessels, C. H. Storry, M. Weel, A. Mullers, and J. Walz.

Using electric fields to prevent mirror-trapped antiprotons in antihydrogen studies. Physical Review. A **87**, 023422 (2013). DOI: 10.1103/PhysRevA.87.023422.

[44] Jack W. Ekin. *Experimental Techniques for low temperature measurements: Cryostat Design, Material Properties, and Superconductor Critical-Current Testing p41.* Published by Oxford University Press. First Printing 2006, Second Printing 2007, Third Printing 2007, Fourth Printing 2011.